Towards a Computational Framework for Modeling the Impact of Aortic Coarctations upon Left Ventricular Load

Elias Karabelas[1], Matthias A. F. Gsell[1], Christoph M. Augustin[1,2], Laura Marx[1], Aurel Neic[1], Anton J. Prassl[1], Leonid Goubergrits[3,4], Titus Kuehne[3,4], and Gernot Plank[1,*]

[1]Institute of Biophysics, Medical University of Graz, Graz, Austria
[2]Shadden Research Group, Department of Mechanical Engineering, University of California, Berkeley, CA, USA
[3]Department of Congenital Heart Disease/Pediatric Cardiology, German Heart Institute Berlin, Berlin, Germany
[4]Institute for Imaging Science and Computational Modelling in Cardiovascular Medicine, Charité-Universitätsmedizin Berlin, Berlin, Germany
*Correspondance: Gernot Plank, Medical University of Graz, Institute of Biophysics, Neue Stiftingtalstrasse 6, 8010 Graz, Austria.
gernot.plank@medunigraz.at

Abstract

Computational fluid dynamics (CFD) models of blood flow in the left ventricle (LV) and aorta are important tools for analyzing the mechanistic links between myocardial deformation and flow patterns. Typically, the use of image-based kinematic CFD models prevails in applications such as predicting the acute response to interventions which alter LV afterload conditions. However, such models are limited in their ability to analyze any impacts upon LV load or key biomarkers known to be implicated in driving remodeling processes as LV function is not accounted for in a mechanistic sense.

This study addresses these limitations by reporting on progress made towards a novel electro-mechano-fluidic (EMF) model that represents the entire physics of LV electromechanics (EM) based on first principles. A biophysically detailed finite element (FE) model of LV EM was coupled with a FE-based CFD solver for moving domains using an arbitrary Eulerian-Lagrangian (ALE) formulation. Two clinical cases of patients suffering from aortic coarctations (CoA) were built and parameterized based on clinical data under pre-treatment conditions. For one patient case simulations under post-treatment conditions after geometric repair of CoA by a virtual stenting procedure were compared against pre-treatment results. Numerical stability of the approach was demonstrated by analyzing mesh quality and solver performance under the significantly large deformations of the LV blood pool. Further, computational tractability and compatibility with clinical time scales were investigated by performing strong scaling benchmarks up to 1536 compute cores. The overall cost of the entire workflow for building, fitting and executing EMF simulations was comparable to those reported for image-based kinematic models, suggesting that EMF models show potential of evolving into a viable clinical research tool.

Keywords: cardiac mechanics, computational fluid dynamics, finite element model, arbitrary Lagrangian-Eulerian formulation, patient-specific modeling, translational cardiac modeling, total heart function.

1 Introduction

CFD models of blood flow in the LV and aorta are important tools for analyzing the mechanistic links between myocardial deformation and flow patterns. Typically, such models are either driven by prescribed flow profiles measured in the LV outflow tract or the aortic root [1, 34, 66], or by image-based kinematic models [24, 18, 69, 72, 54, 76] built from segmentation of 4D medical imaging datasets. While such models have proven to be valuable for analyzing the hemodynamic status quo of a patient or for predicting changes in hemodynamics in the aorta secondary to intervention such as aortic valve repair [46] or stenting of a coarctation [35], they are inherently limited in their ability to assess cardiac function as the biophysics driving myocardial activation and deformation is not taken into consideration in the model formulation. EMF models that capture the entire physics of a heartbeat based on first principles show promise to overcome this limitation [20] by rendering feasible the assessment of all essential myocardial parameters, which are known to be key factors driving ventricular remodeling and disease progression. Thus EMF models may offer, in principal, the potential of predicting longer term outcomes beyond changes in the acute response to therapies.

However, due to a number of factors such as the inherent complexity of multiphysics models, the large-scale motion and complex deformation of the myocardial walls as well as the significant computational burden, these models pose substantial methodological challenges. For LV EMF models and similar applications, methods to overcome the problem of large-scale deformations can be roughly classified into two categories: ALE formulations using a moving fluid mesh [22, 62, 79, 78, 83] and immersed boundary (IB) methods [19, 71, 86]. While ALE formulations often rely on severe simplifications or automatic remeshing strategies [51], IB methods are more versatile as the moving wall of the ventricle is not explicitly tracked. However, IBs and all related non-boundary-fitting methods have a reduced accuracy for the solution near the fluid-solid structure interface due to interpolation errors, pose severe challenges on the implementation, and additional degrees of freedom have to be introduced on interface cut elements, which all contributes to significantly higher computational costs [82].

In this study, we report on the progress made towards a novel EMF model of the human LV that is entirely based on first principles and that copes with significantly large defomations, i.e., ejection fractions (EFs) beyond 60 %, without requiring remeshing or IB principles. Validated *in silico* models taken from a recent clinical modeling study where a cohort of *in silico* EM LV and aorta models of patients suffering from aortic valve disease (AVD) and/or CoA [5] were built, served as kinematic driver to a computational model of hemodynamics in the LV cavity and aorta. A hybrid two stage modeling approach was adopted with regard to hemodynamics. First, the afterload imposed by the circulatory system onto the LV was represented by a lumped model of afterload and coupled to an EM model of LV and aorta to compute LV kinematics. Subsequently a full-blown CFD model with moving domain boundaries based on an ALE formulation was *unidirectionally* or *weakly* coupled to the EM model using the kinematics of its endocardial surface as input. We show validation results for two selected clinical CoA cases under pre-treatment conditions and compare pre-treatment and post-treatment simulation results for one patient case in which the CoA was geometrically repaired by a virtual stenting procedure. Further, we demonstrate numerical feasibility of the implemented approach by analyzing changes in mesh quality and its impact upon solver performance under the significantly large deformations of the LV blood pool mesh and also provide strong scaling benchmarking results for a range of 96 to 1536 compute cores. The overall cost of the entire workflow for building, fitting and execution of EMF simulations is $\approx$ 48 hours which is comparable to plain image-based kinematic driver models [55].

2 Methods

The methodology to develop a coupled model of cardiac and cardiovascular hemodynamics based on an ALE formulation is structured as follows.

i) We begin in Section 2.1 by describing MRI data acquisition and anatomical FE model gen-

eration of the LV and aorta for two patients suffering from CoA.

ii) Then, a brief summary of all model components is given comprising an electrophysiology (EP) model to drive electrical activation and repolarization (Section 2.2.1); an EM model describing passive biomechanics as well as the generation of active stresses (Section 2.2.2); afterload models to provide appropriate boundary conditions on the LV endocardium during the ejection phase (Section 2.2.3); and a CFD model with moving domain boundaries representing blood flow in the LV and aorta during ejection. The EM and CFD model are weakly coupled in a forward fluid structure interaction (FSI) framework, where the EM model is used as a kinematic driver to move the fluid domain (Section 2.3).

iii) The solution procedure and software implementation details are outlined in Section 2.4.

iv) Finally, procedures implemented for the patient-specific parameterization of the major model components is described in Section 2.5.

2.1 Clinical data acquisition and model generation

Hemodynamic data of two patients with clinical indication for catheterization due to CoA – all preceding a cardiac magnetic resonance study – were acquired before and after CoA treatment by stent implant, see Table 1. CoA treatment indicators included an echocardiographic measured, peak systolic pressure gradient across the stenotic region of $> 20\,\mathrm{mmHg}$ and/or arterial hypertension. The study was approved by the institutional research ethics committee following the ethical guidelines of the 1975 Declaration of Helsinki. Written informed consent was obtained from the participants' guardians. Acquired data are summarized in Table 1.

2.1.1 MRI acquisition and post processing

MR imaging was done with a whole body 1.5 Tesla MR scanner Achieva R 3.2.2.0 using a five-element cardiac phased-array coil (Philips Medical System, Best, Netherlands). Three MRI sequences were used further in our study: i) flow-sensitive four-dimensional (4D) velocity-encoded magnetic resonance imaging (4D VEC-MRI), ii) three-dimensional (3D) anatomical imaging of the whole heart (3DWH) during diastasis, and iii) 4D gapless short axis Cine MRI.

4D VEC-MRI of the thorax was performed using an anisotropic 4D segmented k-space phase contrast gradient echo sequence. Retrospective electrocardiographic gating without navigator gating of respiratory motion in order to minimize acquisition time was used. Sequence parameters were: acquired voxel $2.5 \times 2.5 \times 2.5\,\mathrm{mm}$; reconstructed voxel $1.7 \times 1.7 \times 2.5\,\mathrm{mm}$; repetition time $3.5\,\mathrm{ms}$; echo time $2.2\,\mathrm{ms}$; flip angle $5°$; 25 reconstructed cardiac phases; number of signal averages 1; High velocity encoding (3 to $6\,\mathrm{m/s}$) in all three directions was used in order to avoid phase wraps in the presence of coarctation and associated secondary flow. Flow measurements were completed with automatic correction of concomitant phase errors. Postprocessing for analysis of flow rates across the aortic valve was carried out with GTFlow 1.6.8 software[1] (Gyrotools, Zurich, Switzerland).

The 3DWH exemplary sequence parameters were: acquired voxel $0.66 \times 0.66 \times 3.2\,\mathrm{mm}$; reconstructed voxel $0.66 \times 0.66 \times 1.6\,\mathrm{mm}$; repetition time $4.0\,\mathrm{ms}$; echo time $2.0\,\mathrm{ms}$; flip angle $90°$; and number of signal averages 3.

Short axes Cine imaging data were acquired with sequence parameters: 16 slices, with an acquisition resolution of $0.86 \times 0.86 \times 6.0$ mm, repetition time 4.24 ms, echo time 2.12 ms, flip angle $60°$ and 25 automatically reconstructed cardiac phases which were used to determine LV volume traces. The non-compact myocardium as well as papillary muscles were counted towards blood pool volume.

[1] `http://www.gyrotools.com/products/gt-flow.html`

MRI based pressure mapping allowing to assess non-invasively the relative pressures in a vessel by solving Pressure Poisson equation (PPE) was done with MevisFlow[2]. Briefly, the PPE can be derived from the Navier–Stokes equations by taking the divergence of the momentum equation (25), see [36, 49] for more details. The processing and analysis pipeline of the pressure mapping consists of the following four steps.

i) Semi-automatic segmentation (labeling) of the aortic domain from 3DWH data generating 3D mask of the aorta.

ii) Background phase correction and phase-unwrapping of the 4D VEC-MRI data and generation of a sequence of volumetric velocity vector fields.

iii) Coarse semi-automatic segmentation of the aorta based on magnitude and phase contrast of the 4D VEC-MRI data and registration with 3DWH based mask of the aorta.

iv) Solving the PPE at each time step having 4D VEC-MRI data as input. Furthermore, a 5 % mask size reduction is applied in order to avoid numerical inconsistencies close to the vessel wall as suggested earlier [53].

Relative pressure maps are represented with zero pressure located at the center of the CoA (narrowest location). 3D mask based on 3DWH data was used due to its better spatial resolution compared to 4D VEC-MRI data. Correction of velocity data (step ii) was done in order to minimize noise and aliasing artifacts originating from multiple sources.

2.1.2 Invasive catheter recordings

During catheterization, pressure was recorded over the cardiac cycle in the ascending aorta and the LV before treatment and repeated in the ascending aorta after an interventional treatment procedure was performed. Pressures were recorded simultaneously at three predefined locations (LV, ascending aorta, and descending aorta) and the femoral artery during catheterization. Patients were sedated by intravenous administration of a bolus of midazolam (0.1 to 0.2 mg/kg, max. 5 mg), followed by a bolus of propofol (1 to 2 mg/kg, as needed) and continuous infusion of propofol (approximately 4 mg/kg/h, as needed). Pressure measurements were taken with senior cardiologists present. Pigtail catheters (Cordis, Warren, NJ, USA) of 5-6F were connected to pressure transducers (Becton-Dickinson, Franklin Lakes, NJ, USA). Routinely, patients received balloon angioplasty with or without additional placement of a stent in order to treat a given stenosis by removing the narrowing of the vessel and thus the pressure gradient. To reduce duration of catheterization, pressures were measured post-treatment only in the ascending aorta. The Schwarzer hemodynamic analysis system (Schwarzer, Heilsbronn, Germany) was used to amplify, acquire, and analyze pressure signals.

2.1.3 Anatomical FE Model Generation

Multi-label segmentation of the LV myocardium, LV blood pool, left atrium (LA) and aortic cavities was done at the DHZB using 3DWH data and the ZIB Amira software[3] [74]. The segmentations were smoothed and upsampled to a 0.1 mm isotropic resolution using a variational smoothing method [20]. The resulting high resolution multi-label segmentation was meshed using CGAL[4] [81], giving a global mesh $\Omega^0_{\text{s,total}}$ consisting of tetrahedral elements. Here, $(\bullet)^0$ denotes the mechanical reference configuration at end-diastolic pressure. The mesh was subdivided into various subdomains corresponding to predefined labels which are summarized in Table 2. We write

$$\Omega^0_{\text{s,total}} = \bigcup_{i \in I} \Omega^0_{\text{s},i}, \tag{1}$$

[2] `https://www.mevis.fraunhofer.de/en/solutionpages/mevisflow-non-invasive-interactive-exploration-of-in-vivo-hemodynamics.html`

[3] `https://amira.zib.de`

[4] `http://www.cgal.org`

with the index set

$$I := \{\mathrm{lv}, \mathrm{ao}, \mathrm{cushion}, \mathrm{av}, \mathrm{mv}, \mathrm{lvbp}, \mathrm{aobp}\}, \tag{2}$$

see Figure 1 (E–G) for illustration. With this, we define the following submeshes

$$\Omega^0_{\mathrm{s}} := \Omega^0_{\mathrm{s,total}} \setminus \left(\Omega^0_{\mathrm{s,lbvp}} \cup \Omega^0_{\mathrm{s,aobp}}\right), \tag{3}$$

$$\Omega^0_{\mathrm{s,bp}} = \widetilde{\Omega}^0_f := \Omega^0_{\mathrm{s,av}} \cup \Omega^0_{\mathrm{s,lvbp}} \cup \Omega^0_{\mathrm{s,aobp}}, \tag{4}$$

where Ω^0_{s} is the solid domain and $\Omega^0_{\mathrm{s,bp}}$ is the unsmoothed blood pool domain used for extracting a smoothed CFD mesh, see Figure 1 (E) and (F). For later use, we define the following surfaces

$$\Gamma^0_{\mathrm{s,N}} := \partial\left(\left(\Omega^0_{\mathrm{s,lv}} \cup \Omega^0_{\mathrm{s,av}} \cup \Omega^0_{\mathrm{s,mv}}\right) \cap \Omega^0_{\mathrm{s,lvbp}}\right), \tag{5}$$

$$\Gamma^0_{\mathrm{s,H}} := \partial\Omega^0_{\mathrm{s}} \setminus \left(\Gamma^0_{\mathrm{s,N}} \cup \Gamma^0_{\mathrm{s,D}}\right), \tag{6}$$

$$\Gamma^0_{\mathrm{s,bp}} := \partial\Omega^0_{\mathrm{s,bp}} \setminus \Gamma^0_{\mathrm{s,D}}, \tag{7}$$

where $\Gamma^0_{\mathrm{s,D}}$ denote the cutoff faces as indicated by blue lines in Figure 1; $\Gamma^0_{\mathrm{s,N}}$ are surfaces subject to pressure; and $\Gamma^0_{\mathrm{s,H}}$ are surfaces with homogeneous Neumann boundary conditions. In order to avoid numerical difficulties with non-smooth, jagged boundaries, the surface of the mechanical blood pool domain $\Gamma^0_{\mathrm{s,bp}}$ was extracted and smoothed using the VMTK toolbox[5] [2]. The smoothed surface, $\Gamma^0_{\mathrm{f,wall}}$, was used to define the boundary of the fluid domain reference configuration, Ω^0_{f}, for volumetric FE meshing using ANSYS ICEM CFD[6]. Refined boundary layers were included in this process to better resolve sharp gradients in the vicinity of $\Gamma^0_{\mathrm{f,wall}}$ occurring during simulation of hemodynamics. The various processing stages for building EM and CFD models are illustrated in Figures 1 and 4, respectively.

2.2 Electromechanical Model

2.2.1 Electrophysiology of the LV

A recently developed reaction-eikonal (R-E) model [58] was employed to generate electrical activation sequences which serve as a trigger for active stress generation in cardiac tissue. The hybrid R-E model combines a standard reaction-diffusion (R-D) model based on the monodomain equation with an eikonal model. Briefly, the eikonal equation is given as

$$\begin{cases} \sqrt{\nabla_{\mathbf{X}} t_{\mathrm{a}}^{\top}\, \mathbf{V}\, \nabla_{\mathbf{X}} t_{\mathrm{a}}} &= 1 \quad \text{in } \Omega^0_{\mathrm{s,lv}}, \\ t_{\mathrm{a}} &= t_0 \quad \text{on } \Gamma^0_{\mathrm{s},*}, \end{cases} \tag{8}$$

where $(\nabla_{\mathbf{X}})$ is the gradient with respect to the end-diastolic reference configuration $\Omega^0_{\mathrm{s,lv}}$; t_{a} is a positive function describing the wavefront arrival time at location $\mathbf{X} \in \Omega^0_{\mathrm{s,lv}}$; and t_0 are initial activations at locations $\Gamma^0_{\mathrm{s},*} \subseteq \Gamma^0_{\mathrm{s,N}}$. The symmetric positive definite 3×3 tensor $\mathbf{V}(\mathbf{X})$ holds the squared velocities $(v_{\mathrm{f}}(\mathbf{X}), v_{\mathrm{s}}(\mathbf{X}), v_{\mathrm{n}}(\mathbf{X}))$ associated to the tissue's eigenaxes, referred to as fiber, $\mathbf{f}_0$, sheet, $\mathbf{s}_0$, and sheet normal, $\mathbf{n}_0$, orientations. The arrival time function $t_{\mathrm{a}}(\mathbf{X})$ was subsequently used in a modified monodomain R-D model given as

$$\beta C_{\mathrm{m}} \frac{\partial V_{\mathrm{m}}}{\partial t} = \nabla_{\mathbf{X}} \cdot \boldsymbol{\sigma}_{\mathrm{i}} \nabla_{\mathbf{X}} V_{\mathrm{m}} + I_{\mathrm{foot}} - \beta I_{\mathrm{ion}}, \tag{9}$$

where an arrival time dependent foot current, $I_{\mathrm{foot}}(t_{\mathrm{a}})$, was added which is designed to mimic subthreshold electrotonic currents to produce a physiological foot of the action potential. The key advantage of the R-E model is its ability to compute activation sequences at much coarser spatial resolutions that are not afflicted by the spatial undersampling artifacts leading to conduction slowing or even numerical conduction block as it is observed in standard R-D models. Ventricular EP was represented by the tenTusscher–Noble–Noble–Panfilov model of the human ventricular myocyte [80]. As indicated in Equations (8, 9), activation sequences and electrical source distribution in the LV were computed in its end-diastolic configuration $\Omega^0_{\mathrm{s,lv}}$, that is, any effects of deformation upon electrotonic currents remained unaccounted for.

[5] `http://www.vmtk.org`

[6] `http://www.ansys.com/Services/training-center/platform/introduction-to-ansys-icem-cfd-Hexa`

2.2.2 Active and Passive Mechanics in the LV and Aorta

The deformation of the heart is governed by imposed external loads such as pressure in the cavities or from surrounding tissue and active stresses intrinsically generated during contraction. Tissue properties of the LV myocardium and the aorta are characterized as a hyperelastic, nearly incompressible, anisotropic material with a non-linear stress-strain relationship. Mechanical deformation was described by Cauchy's equation of motion under stationary equilibrium assumptions leading to a quasi-static boundary value problem

$$-\nabla_{\mathbf{X}} \cdot \mathbf{F}\mathbf{S}(\mathbf{d}_{\mathrm{s}}, t) = \mathbf{0} \quad \text{in } \Omega^0_{\mathrm{s}}, \tag{10}$$

for $t \in [0, T]$, where $\mathbf{d}_{\mathrm{s}}$ is the unknown displacement; $\mathbf{F}$ is the deformation gradient; $\mathbf{S}$ is the second Piola–Kirchhoff stress tensor; and $(\nabla_{\mathbf{X}} \cdot)$ denotes the divergence operator in the Lagrange reference configuration. Homogeneous Dirichlet boundary conditions

$$\mathbf{d}_{\mathrm{s}} = \mathbf{0} \quad \text{on} \quad \Gamma^0_{\mathrm{s,D}}, \tag{11}$$

homogeneous Neumann boundary conditions

$$\mathbf{F}\mathbf{S}(\mathbf{d}_{\mathrm{s}}, t)\, \mathbf{n}_{\mathrm{s},0} = \mathbf{n}_{\mathrm{s},0} \quad \text{on} \quad \Gamma^0_{\mathrm{s,H}}, \tag{12}$$

and inhomogeneous Neumann boundary conditions

$$\mathbf{F}\mathbf{S}(\mathbf{d}_{\mathrm{s}}, t)\, \mathbf{n}_{\mathrm{s},0} = p(t) J\, \mathbf{F}^{-\top}(\mathbf{d}_{\mathrm{s}}, t)\, \mathbf{n}_{\mathrm{s},0} \quad \text{on} \quad \Gamma^0_{\mathrm{s,N}} \tag{13}$$

were imposed, where $\mathbf{n}_{\mathrm{s},0}$ is the outward unit normal vector; $p(t)$ is the pressure; and $J = \det \mathbf{F}$. For sake of clarity, boundary conditions are illustrated in Figure 1 (C).

The total stress $\mathbf{S}$ was additively decomposed according to

$$\mathbf{S} = \mathbf{S}_{\mathrm{pas}} + \mathbf{S}_{\mathrm{act}}, \tag{14}$$

where $\mathbf{S}_{\mathrm{pas}}$ and $\mathbf{S}_{\mathrm{act}}$ refer to the passive and active stresses, respectively. Passive stresses were modeled based on the constitutive equation

$$\mathbf{S}_{\mathrm{pas}} = 2\frac{\partial \Psi(\mathbf{C})}{\partial \mathbf{C}} \tag{15}$$

given a hyper-elastic strain-energy function Ψ and the right Cauchy–Green strain tensor $\mathbf{C} = \mathbf{F}^{\top}\mathbf{F}$. Two different strain-energy functions were used for characterizing passive mechanical behavior in the LV and the aorta. In the LV, where the underlying mesh $\Omega^0_{\mathrm{s,lv}}$ and fiber orientations $(\mathbf{f}_0, \mathbf{s}_0, \mathbf{n}_0)$ are the same as for the EP model, Section 2.2.1, the transversely isotropic constitutive relation

$$\Psi_{\mathrm{Guc}}(\mathbf{C}) = \frac{\kappa}{2}(\log J)^2 + \frac{C_{\mathrm{Guc}}}{2}\left[\exp(\mathcal{Q}) - 1\right]. \tag{16}$$

by Guccione et al. [38] was employed. Here, the term in the exponent is

$$\mathcal{Q} = b_{\mathrm{f}}(\mathbf{f}_0 \cdot \overline{\mathbf{E}}\mathbf{f}_0)^2 + b_{\mathrm{t}}\left[(\mathbf{s}_0 \cdot \overline{\mathbf{E}}\mathbf{s}_0)^2 + (\mathbf{n}_0 \cdot \overline{\mathbf{E}}\mathbf{n}_0)^2 + 2(\mathbf{s}_0 \cdot \overline{\mathbf{E}}\mathbf{n}_0)^2\right] + 2b_{\mathrm{fs}}\left[(\mathbf{f}_0 \cdot \overline{\mathbf{E}}\mathbf{s}_0)^2 + (\mathbf{f}_0 \cdot \overline{\mathbf{E}}\mathbf{n}_0)^2\right] \tag{17}$$

and $\overline{\mathbf{E}} = \frac{1}{2}(\overline{\mathbf{C}} - \mathbf{I})$ is the modified isochoric Green–Lagrange strain tensor, where $\overline{\mathbf{C}} := J^{-2/3}\mathbf{C}$. Default values of $b_{\mathrm{f}} = 18.48$, $b_{\mathrm{t}} = 3.58$, and $b_{\mathrm{fs}} = 1.627$ were used. The parameter C_{Guc} was varied for the different cases, see Table 3. In the aorta $\Omega^0_{\mathrm{s,ao}}$, unlike in previous studies [4], we refrained from assigning fiber structures, since our efforts were primarily focused on modeling the biomechanics of the LV and, to a lesser degree, the aorta. Thus, in absence of information on structural anisotropy, an isotropic model due to Demiray [23] was used

$$\Psi_{\mathrm{Dem}}(\mathbf{C}) := \frac{\kappa}{2}(\log J)^2 + \frac{a}{2\,b}\left\{\exp\left[b\left(\mathrm{tr}(\overline{\mathbf{C}}) - 3\right)\right] - 1\right\}. \tag{18}$$

The parameter $\widetilde{C} = \frac{a}{2b}$ was chosen such that $\widetilde{C} = 3000\,\text{kPa}$ in the aorta, $\widetilde{C} = 30\,000\,\text{kPa}$ for valves, and $\widetilde{C} = 300\,\text{kPa}$ for the elastic cushion. The bulk modulus κ, which serves as a penalty parameter to enforce nearly incompressible material behavior, was chosen as $\kappa = 650\,\text{kPa}$ in both Equations (16, 18). For the elastic cushion a value of $\kappa = 100\,\text{kPa}$ was used.

A simplified phenomenological contractile model was used to represent active stress generation [61]. Owing to its small number of parameters and its direct relation to clinically measurable quantities such as peak pressure, p_{lv}, and the maximum rate of rise of pressure, $\mathrm{d}p_{\text{lv}}/\,\mathrm{d}t_{\text{max}}$, this model is fairly easy to fit and thus very suitable for being used in clinical EM modeling studies. Briefly, the active stress transient is given by

$$S_{\text{a}}(t,\lambda) = S_{\text{peak}}\,\phi(\lambda)\,\tanh^2\left(\frac{t_{\text{s}}}{\tau_{\text{c}}}\right)\tanh^2\left(\frac{t_{\text{dur}}-t_{\text{s}}}{\tau_{\text{r}}}\right), \qquad \text{for } 0 < t_{\text{s}} < t_{\text{dur}}, \tag{19}$$

with

$$\phi = \tanh(\text{ld}(\lambda-\lambda_0)), \quad \tau_{\text{c}} = \tau_{\text{c}_0} + \text{ld}_{\text{up}}(1-\phi), \quad t_{\text{s}} = t - t_{\text{a}} - t_{\text{emd}} \tag{20}$$

and t_{s} is the onset of contraction; $\phi(\lambda)$ is a non-linear length-dependent function in which λ is the fiber stretch and λ_0 is the lower limit of fiber stretch below which no further active tension is generated; t_{a} is the local activation time from Eq. (8); t_{emd} is the EM delay between the onsets of electrical depolarization and active stress generation; S_{peak} is the peak isometric tension; t_{dur} is the duration of active stress transient; τ_{c} is time constant of contraction; τ_{c_0} is the baseline time constant of contraction; ld_{up} is the length-dependence of τ_{c}; τ_{r} is the time constant of relaxation; and ld is the degree of length dependence. Thus, active stresses in this simplified model are only length-dependent, but dependence on fiber velocity, $\dot{\lambda}$, is ignored. Unlinke in previous studies [61] we set the nonlinear length-dependent function $\phi(\lambda) = 1$ for the whole simulation. The active stress tensor in the reference configuration $\Omega^0_{\text{s,lv}}$ induced in fiber direction $\mathbf{f}_0$ is defined as

$$\mathbf{S}_{\text{a}} = S_{\text{a}}\left(\mathbf{f}_0 \cdot \mathbf{C}\mathbf{f}_0\right)^{-1}\mathbf{f}_0 \otimes \mathbf{f}_0, \tag{21}$$

with S_a defined in Equation (19). This active stress involves a scaling by $\lambda^2 = \mathbf{f}_0 \cdot \mathbf{C}\mathbf{f}_0$, see [63] for details.

2.2.3 Mechanical and Hemodynamic Afterload Models

Hydrostatic pressures in the LV, p_{lv}, and the proximal aorta, p_{ao}, were modeled using a 3-element Windkessel model [88], and the system of PDEs (10) was linked to this lumped model of the arterial system, see Figure 2. The models were coupled by a diode (aortic valve) which opens at the end of the isovolumetric contraction (IVC) phase when the pressure in the LV cavity, p_{lv}, exceeds the pressure in the proximal aorta, p_{ao}, and closes at the end of ejection when p_{lv} drops below p_{ao} and the flow q_{lv} starts to reverse. In its open state the aortic valve was modeled as a linear resistor, R_{av}, in series with the characteristic impedance of the aorta, Z_{c}. During ejection, the pressure in the LV was then computed by the Windkessel equation

$$\frac{\mathrm{d}p_{\text{lv}}}{\mathrm{d}t} = \frac{1}{C}\left(1 + \frac{Z_{\text{c}} + R_{\text{av}}}{R}\right)q_{\text{lv}} + (Z_{\text{c}} + R_{\text{av}})\frac{\mathrm{d}q_{\text{lv}}}{\mathrm{d}t} - \frac{1}{RC}\,p_{\text{lv}}, \tag{22}$$

which predicts the rate of change of pressure in the LV as a function of flow q_{lv} out of the LV into the aorta. The resistor R represents peripheral arterial resistance placed in parallel with a capacitor C, representing vascular compliance.

A similar form of Equation (22) was also used to estimate the pressure in the aorta, p_{ao}. In this case, there is no additional resistance due to an outlet valve and hence R_{av} is omitted. Balancing of the PDE (10) and the ODE (22) was achieved by recasting Equation (10) as a saddle point problem, see [39, 40].

For CFD simulations, hydrostatic pressures at artificial aortic fluid outlets, were modeled using a similar 3-element Windkessel model as in Equation (22) that was rewritten in the form of the

following differential algebraic equations for outlet i

$$C_i \frac{\mathrm{d}p_{\mathrm{d},i}}{\mathrm{d}t} + \frac{p_{\mathrm{d},i}}{R_i} = q_i, \tag{23}$$

$$p_{\mathrm{wk},i} = Z_i q_i + p_{\mathrm{d},i}, \tag{24}$$

see [31, 13] for more details. During ejection the Windkessel pressure p_{wk} at an outlet was then applied as an outflow boundary condition for the fluid flow model, see Section 2.5.5. In Equations (23, 24), C_i represents compliance, Z_i impedence, and R_i resistance of the peripheral arteries for the respective aortic outlet and q_i denotes the flux through this outlet. Fitting of the parameters involved will be discussed in Section 2.5.5.

2.3 Fluid flow model

Human blood in larger vessels such as the LV or the aorta complies with the assumptions of an incompressible, isothermal, Newtonian and single-phase liquid [59]. Let $\Omega_{\mathrm{f}} \subsetneq \mathbb{R}^3$ denote the fluid domain, then the evolution of flow is governed by the incompressible Navier–Stokes equations

$$\rho_{\mathrm{f}} \left(\frac{\partial}{\partial t}\mathbf{u}_{\mathrm{f}} + \mathbf{u}_{\mathrm{f}} \cdot \nabla_{\mathbf{x}} \mathbf{u}_{\mathrm{f}} \right) - \nabla_{\mathbf{x}} \cdot \boldsymbol{\sigma}_{\mathrm{f}}(\mathbf{u}_{\mathrm{f}}, p_{\mathrm{f}}) = \mathbf{0} \qquad \text{in } \Omega_{\mathrm{f}}, \tag{25}$$

$$\nabla_{\mathbf{x}} \cdot \mathbf{u}_{\mathrm{f}} = 0 \qquad \text{in } \Omega_{\mathrm{f}}, \tag{26}$$

$$\mathbf{u}_{\mathrm{f}} = \mathbf{0} \qquad \text{on } \Gamma_{\mathrm{noslip}}, \tag{27}$$

$$\mathbf{u}_{\mathrm{f}} = \mathbf{g}_{\mathrm{f}} \qquad \text{on } \Gamma_{\mathrm{inflow}}, \tag{28}$$

$$\boldsymbol{\sigma}_{\mathrm{f}} \mathbf{n}_{\mathrm{f}} - \rho_{\mathrm{f}} \beta \left(\mathbf{u}_{\mathrm{f}} \cdot \mathbf{n}_{\mathrm{f}}\right)_{-} \mathbf{u}_{\mathrm{f}} = -p_{\mathrm{wk}} \mathbf{n}_{\mathrm{f}} \qquad \text{on } \Gamma_{\mathrm{outflow}}, \tag{29}$$

$$\mathbf{u}_{\mathrm{f}}\big|_{t=0} = \mathbf{u}_0, \tag{30}$$

where $\mathbf{u}_{\mathrm{f}}$ denotes fluid velocity; p_{f} is fluid pressure; ρ_{f} is the density of blood; $\boldsymbol{\sigma}_{\mathrm{f}}$ is the fluid stress tensor; $\mathbf{g}_{\mathrm{f}}$ is a velocity inlet; p_{wk} is the Windkessel pressure solution to Equations (23, 24); $\mathbf{u}_0$ refers to the initial condition; $\mathbf{n}_{\mathrm{f}}$ is the outward normal of the fluid domain; and $(\nabla_{\mathbf{x}})$ is the gradient and $(\nabla_{\mathbf{x}}\cdot)$ is the divergence operator in the fluid domain Ω_{f}. The sets Γ_{noslip}, Γ_{inflow}, and $\Gamma_{\mathrm{outflow}}$ denote the complementary subsets of $\Gamma_{\mathrm{f}} := \partial\Omega_{\mathrm{f}}$ and we assume that $|\Gamma_{\mathrm{outflow}}| > 0$. Note that Equation (28) is given only for the sake of completeness but was not used in this study, as the inflow of blood into the aorta is driven by the motion of the LV thus avoiding the need for prescribing an inflow profile as it is necessary in models which consider the aorta in isolation. For $p_{\mathrm{wk}} \equiv 0$, boundary condition (29) is referred to as *directional do-nothing boundary condition* [28, 16] and the term

$$\left(\mathbf{u}_{\mathrm{f}} \cdot \mathbf{n}_{\mathrm{f}}\right)_{-} := \frac{1}{2}\left(\mathbf{u}_{\mathrm{f}} \cdot \mathbf{n}_{\mathrm{f}} - |\mathbf{u}_{\mathrm{f}} \cdot \mathbf{n}_{\mathrm{f}}|\right) \tag{31}$$

is added for backflow stabilization. A value of $\beta > \frac{1}{2}$ was assumed to guarantee stability of the system. However, in practical applications values of $\beta \leq \frac{1}{2}$ were also used without causing numerical issues, see [28]. All physical parameters in Equations (25)–(30) are summarized in Table 4. In presence of multiple outlets outflow boundary conditions as given in Equation (29) were prescribed at each of the outlets.

2.3.1 Extension to Moving Geometries

For time-dependent fluid domains, i.e., $\Omega_{\mathrm{f}} = \Omega_{\mathrm{f}}^t$, Equations (25)–(30) need to be modified to account for the domain movement. This requires the linking of the equations governing fluid dynamics – posed in an Eulerian coordinate frame – with the structural mechanics equations – posed in a Lagrangian reference frame. This is achieved by using the ALE formulation which combines both Lagrangian and Eulerian formulation in a generalized description, see [12, Section 1.3] and [41]. Similar to structural mechanics, a reference fluid configuration $\Omega_{\mathrm{f}}^0 \subsetneq \mathbb{R}^3$ is used which we identify with the mesh been generated at end-diastolic state, see Section 2.1.3. The

coordinate system of the Eulerian frame is denoted by $\mathbf{x}$ and the reference coordinate system is denoted by $\mathbf{X}$. Their relation is given by the ALE mapping $\mathbf{x} = \mathbf{X} + \mathbf{d}_\mathrm{f}(t, \mathbf{X})$. Here, $\mathbf{d}_\mathrm{f}(t, \mathbf{X})$ refers to an arbitrary, not necessarily physical, displacement of points to track the deformation of the fluid domain. Using this ALE mapping the time-dependent moving fluid domain is represented as

$$\Omega_\mathrm{f}^t := \left\{ \mathbf{x} : \mathbf{x} = \mathbf{X} + \mathbf{d}_\mathrm{f}(t, \mathbf{X}),\, \forall \mathbf{X} \in \Omega_\mathrm{f}^0 \right\}. \tag{32}$$

Further, we define the fluid domain velocity $\mathbf{w}_\mathrm{f}$ as

$$\mathbf{w}_\mathrm{f} := \frac{\partial}{\partial t} \mathbf{d}_\mathrm{f} \big|_{\mathbf{X}}, \tag{33}$$

where $\frac{\partial}{\partial t}(\cdot)\big|_{\mathbf{X}}$ is the derivative with respect to t with $\mathbf{X}$ being fixed, and the moving interface between fluid and solid domain as

$$\Gamma_{\mathrm{f,mov}}^t := \partial \Omega_\mathrm{f}^t \setminus \bigcup_{i=1}^{n_\mathrm{outlets}} \Gamma_{\mathrm{f,outflow},i}^t, \tag{34}$$

where $\Gamma_{\mathrm{f,outflow},i}^t$ are the individual aortic outlets. The fluid displacement at this point remains unknown and will be specified in Section 2.3.3. Combining these concepts, an ALE description of the Navier–Stokes equations can be derived, see, e.g., [12, 29],

$$\rho_\mathrm{f} \left(\frac{\partial}{\partial t} \mathbf{u}_\mathrm{f} \big|_{\mathbf{X}} + (\mathbf{u}_\mathrm{f} - \mathbf{w}_\mathrm{f}) \cdot \nabla_{\mathbf{x}} \mathbf{u}_\mathrm{f} \right) - \nabla_{\mathbf{x}} \cdot \boldsymbol{\sigma}_\mathrm{f}(\mathbf{u}_\mathrm{f}, p_\mathrm{f}) = \mathbf{0} \qquad \text{on } \Omega_\mathrm{f}^t, \tag{35}$$

$$\nabla_{\mathbf{x}} \cdot \mathbf{u}_\mathrm{f} = 0 \qquad \text{on } \Omega_\mathrm{f}^t, \tag{36}$$

$$\mathbf{u}_\mathrm{f} = \mathbf{g}_\mathrm{mov} \qquad \text{on } \Gamma_{\mathrm{f,mov}}^t, \tag{37}$$

$$\boldsymbol{\sigma}_\mathrm{f}(\mathbf{u}_\mathrm{f}, p_\mathrm{f}) \mathbf{n}_\mathrm{f} - \rho_\mathrm{f} \beta ((\mathbf{u}_\mathrm{f} - \mathbf{w}_\mathrm{f}) \cdot \mathbf{n}_\mathrm{f})_- \mathbf{u}_\mathrm{f} = -p_{\mathrm{wk,i}} \mathbf{n}_\mathrm{f} \qquad \text{on each } \Gamma_{\mathrm{f,outflow},i}^t, \tag{38}$$

$$\mathbf{u}_\mathrm{f} \big|_{t=0} = \mathbf{u}_0 \qquad \text{in } \Omega_\mathrm{f}^0. \tag{39}$$

Along $\Gamma_{\mathrm{f,mov}}^t$ we imposed equality between fluid velocity and the velocity of the moving surfaces. Boundary condition (38) is the ALE equivalent of the outflow stabilization in Equation (29), see [12, Section 8.4.2.3]. Details on how domain movement and velocity were chosen in our application will be discussed later in Sections 2.3.3 and 2.5.5.

2.3.2 Variational Formulation of the Navier–Stokes equations

Following [11, 12, 64], the discrete variational formulation of the ALE equations (35)–(39) can be stated in the following abstract form: find $\mathbf{u}_\mathrm{f}^\mathrm{h} \in [\mathcal{S}_{\mathrm{h},\mathbf{g}}^1(\mathcal{T}_\mathrm{N})]^3, p_\mathrm{f}^\mathrm{h} \in \mathcal{S}_\mathrm{h}^1(\mathcal{T}_\mathrm{N})$ such that for all $\mathbf{v}^\mathrm{h} \in [\mathcal{S}_{h,\mathbf{0}}^1(\mathcal{T}_\mathrm{N})]^3$ and for all $q^\mathrm{h} \in \mathcal{S}_\mathrm{h}^1(\mathcal{T}_\mathrm{N})$

$$A_\mathrm{NS}(\mathbf{v}^\mathrm{h}, q^\mathrm{h}; \mathbf{u}_\mathrm{f}^\mathrm{h}, p_\mathrm{f}^\mathrm{h}) + S_\mathrm{VMS}(\mathbf{v}^\mathrm{h}, q^\mathrm{h}; \mathbf{u}_\mathrm{f}^\mathrm{h}, p_\mathrm{f}^\mathrm{h}) = F_\mathrm{NS}(\mathbf{v}^\mathrm{h}), \tag{40}$$

with the classical bilinear form of the Navier–Stokes equations

$$\begin{aligned} A_\mathrm{NS}(\mathbf{v}^\mathrm{h}, q^\mathrm{h}; \mathbf{u}_\mathrm{f}^\mathrm{h}, p_\mathrm{f}^\mathrm{h}) :=& \rho_\mathrm{f} \int_{\Omega_\mathrm{f}^t} \mathbf{v}^\mathrm{h} \cdot \left(\frac{\partial}{\partial t} \mathbf{u}_\mathrm{f}^\mathrm{h} + \left(\mathbf{u}_\mathrm{f}^\mathrm{h} - \mathbf{w}_\mathrm{f}^\mathrm{h} \right) \cdot \nabla_{\mathbf{x}} \mathbf{u}_\mathrm{f}^\mathrm{h} \right) \mathrm{d}\mathbf{x} + \int_{\Omega_\mathrm{f}^t} \boldsymbol{\varepsilon}(\mathbf{v}^\mathrm{h}) : \boldsymbol{\sigma}_\mathrm{f}(\mathbf{u}_\mathrm{f}^\mathrm{h}, p_\mathrm{f}^\mathrm{h}) \, \mathrm{d}\mathbf{x} \\ &+ \int_{\Omega_\mathrm{f}^t} q^\mathrm{h} \nabla_{\mathbf{x}} \cdot \mathbf{u}_\mathrm{f}^\mathrm{h} \, \mathrm{d}\mathbf{x} - \rho_\mathrm{f} \beta \sum_{i=1}^{n_\mathrm{outlets}} \int_{\Gamma_{\mathrm{f,outflow},i}^t} ((\mathbf{u}_\mathrm{f}^\mathrm{h} - \mathbf{w}_\mathrm{f}^\mathrm{h}) \cdot \mathbf{n}_\mathrm{f})_- \mathbf{v}^\mathrm{h} \cdot \mathbf{u}_\mathrm{f}^\mathrm{h} \, \mathrm{d}s_{\mathbf{x}}, \end{aligned} \tag{41}$$

the bilinear form S_VMS, which is explained later in Equation (44), and the right-hand side contribution

$$F_\mathrm{NS}(\mathbf{v}^\mathrm{h}) := - \sum_{i=1}^{n_\mathrm{outlets}} p_{\mathrm{wk,i}} \int_{\Gamma_{\mathrm{f,outflow},i}^t} \mathbf{v}^\mathrm{h} \cdot \mathbf{n}_\mathrm{f} \, \mathrm{d}s_{\mathbf{x}}. \tag{42}$$

In Equation (41), $\boldsymbol{\varepsilon}$ is the strain-rate tensor and $\mathbf{w}_{\mathrm{f}}^{\mathrm{h}}$ is the discrete counterpart of the fluid domain velocity $\mathbf{w}_{\mathrm{f}}$, i.e.,

$$\mathbf{w}_{\mathrm{f}}^{\mathrm{h}}(t^{n+1}, \mathbf{X}) = \frac{\mathbf{d}_{\mathrm{f}}(t^{n+1}, \mathbf{X}) - \mathbf{d}_{\mathrm{f}}(t^{n}, \mathbf{X})}{\Delta t}. \tag{43}$$

The FE function space $\mathcal{S}^1_{\mathrm{h},*}(\mathcal{T}_{\mathrm{N}})$ is the conformal trial space of piecewise linear, globally continuous basis functions over a decomposition $\mathcal{T}_{\mathrm{N}}$ of Ω_{f}^t into N simplicial elements constrained by $\mathbf{v}^{\mathrm{h}} = *$ on essential boundaries. The FE function space $\mathcal{S}^1_{\mathrm{h}}(\mathcal{T}_{\mathrm{N}})$ denotes the same space without constraints. For further details we refer to [17, 75].

From a mathematical point of view, the Navier–Stokes equation can be seen as a multidimensional convectionâĂŞdiffusion equation with pressure acting as a Lagrangian multiplier of the incompressibility constraint. In the common case where velocity and pressure are retained as unknowns, as above, the Ladyzhenskaya–Babuška–Brezzi (LBB) condition has to be satisfied by the velocity and pressure spaces [25]. A violation of the LBB condition may lead to pressure oscillations. Stabilization techniques allowing the circumvention of the LBB condition exist and have been extensively studied, see for example [43, 32, 26, 14]. However, with increasing Reynolds number the Navier–Stokes equations become convection dominated. This requires increasingly finer mesh resolutions to accurately resolve finer flow details which, eventually, renders numerical solution in this form computationally intractable. As a remedy, one can resort to using turbulence models. In particular, in this study the *residual based variational multiscale turbulence model* (RBVMS), see [42, 11, 12, 64] was employed which acts as a stabilization and a turbulence model. The underlying main idea is to split the unknown solution into resolvable (coarse) and unresolvable (fine) scales by the FE approximation, where the finer scale details are taken into account based on element residuals. For details on the derivation we refer to elsewhere [11]. The term S_{VMS} in Equation (40) denotes the bilinear form of the RBVMS formulation and reads as

$$\begin{aligned}
S_{\mathrm{VMS}}(\mathbf{v}^{\mathrm{h}}, q^{\mathrm{h}}; \mathbf{u}_{\mathrm{f}}^{\mathrm{h}}, p_{\mathrm{f}}^{\mathrm{h}}) :=& \frac{1}{\rho_{\mathrm{f}}} \sum_{l=1}^{n_{\mathrm{el}}} \int_{\tau_\ell} \tau_{\mathrm{MOM}} \left(\rho_{\mathrm{f}} \left(\mathbf{u}_{\mathrm{f}}^{\mathrm{h}} - \mathbf{w}_{\mathrm{f}}^{\mathrm{h}} \right) \cdot \nabla_{\mathbf{x}} \mathbf{v}^{\mathrm{h}} + q^{\mathrm{h}} \right) \cdot \mathbf{r}_{\mathrm{MOM}}(\mathbf{u}_{\mathrm{f}}^{\mathrm{h}}, p_{\mathrm{f}}^{\mathrm{h}}) \, \mathrm{d}\mathbf{x} \\
&+ \sum_{l=1}^{n_{\mathrm{el}}} \int_{\tau_\ell} \tau_{\mathrm{CONT}} \nabla_{\mathbf{x}} \cdot \mathbf{v}^{\mathrm{h}} \nabla_{\mathbf{x}} \cdot \mathbf{u}_{\mathrm{f}}^{\mathrm{h}} \, \mathrm{d}\mathbf{x} \\
&- \sum_{l=1}^{n_{\mathrm{el}}} \int_{\tau_\ell} \tau_{\mathrm{MOM}} \mathbf{v}^{\mathrm{h}} \cdot \left(\nabla_{\mathbf{x}} \mathbf{u}_{\mathrm{f}}^{\mathrm{h}} \mathbf{r}_{\mathrm{MOM}}(\mathbf{u}_{\mathrm{f}}^{\mathrm{h}}, p_{\mathrm{f}}^{\mathrm{h}}) \right) \, \mathrm{d}\mathbf{x} \\
&- \frac{1}{\rho_{\mathrm{f}}} \sum_{l=1}^{n_{\mathrm{el}}} \int_{\tau_\ell} \tau_{\mathrm{MOM}}^2 \boldsymbol{\varepsilon}(\mathbf{v}^{\mathrm{h}}) : (\mathbf{r}_{\mathrm{MOM}}(\mathbf{u}_{\mathrm{f}}^{\mathrm{h}}, p_{\mathrm{f}}^{\mathrm{h}}) \otimes \mathbf{r}_{\mathrm{MOM}}(\mathbf{u}_{\mathrm{f}}^{\mathrm{h}}, p_{\mathrm{f}}^{\mathrm{h}})) \, \mathrm{d}\mathbf{x},
\end{aligned} \tag{44}$$

where the vector $\mathbf{r}_{\mathrm{MOM}}$ is defined as

$$\mathbf{r}_{\mathrm{MOM}}(\mathbf{u}_{\mathrm{f}}^{\mathrm{h}}, p_{\mathrm{f}}^{\mathrm{h}}) := \rho_{\mathrm{f}} \left(\frac{\partial}{\partial t} \mathbf{u}_{\mathrm{f}}^{\mathrm{h}} + \left(\mathbf{u}_{\mathrm{f}}^{\mathrm{h}} - \mathbf{w}_{\mathrm{f}}^{\mathrm{h}} \right) \cdot \nabla_{\mathbf{x}} \mathbf{u}_{\mathrm{f}}^{\mathrm{h}} \right) - \nabla_{\mathbf{x}} \cdot \boldsymbol{\sigma}_{\mathrm{f}}(\mathbf{u}_{\mathrm{f}}^{\mathrm{h}}, p_{\mathrm{f}}^{\mathrm{h}}). \tag{45}$$

The definition of the parameters $\tau_{\mathrm{MOM}}, \tau_{\mathrm{CONT}}$ according to [64] is given by

$$\tau_{\mathrm{MOM}} := \min \left\{ \left(\frac{4}{\Delta t^2} + (\mathbf{u}_{\mathrm{f}}^{\mathrm{h}} - \mathbf{w}_{\mathrm{f}}^{\mathrm{h}}) \cdot \mathbf{G} (\mathbf{u}_{\mathrm{f}}^{\mathrm{h}} - \mathbf{w}_{\mathrm{f}}^{\mathrm{h}}) \right)^{-\frac{1}{2}}, \frac{\rho_{\mathrm{f}} C_{\mathrm{M}}}{\mu_{\mathrm{f}} \sqrt{\mathbf{G} : \mathbf{G}}} \right\}, \tag{46}$$

with Δt being the time step size and $\mathbf{G} := \frac{\partial \xi}{\partial \mathbf{x}}^{\top} \mathbf{K} \frac{\partial \xi}{\partial \mathbf{x}}$, where $\frac{\partial \xi}{\partial \mathbf{x}}$ denotes the Jacobian of the mapping from a physical FE to the reference FE, the tensor $\mathbf{K}$ is defined as

$$\mathbf{K} := \frac{1}{2\sqrt[3]{2}} \begin{pmatrix} 3 & -1 & -1 \\ -1 & 3 & -1 \\ -1 & -1 & 3 \end{pmatrix} \tag{47}$$

and the constant $C_{\mathrm{M}} = 0.0285$. Further, the stabilization parameter τ_{CONT} is defined as

$$\tau_{\mathrm{CONT}} := \frac{1}{\tau_{\mathrm{MOM}} \mathbf{g}_{\mathrm{f}} \cdot \mathbf{g}_{\mathrm{f}}}, \tag{48}$$

$$g_{\mathrm{f},i} := \sum_{j=1}^{3} \left(\frac{\partial \xi}{\partial \mathbf{x}} \right)_{ji}. \tag{49}$$

2.3.3 EM-based Kinematic driver model

Displacements computed with the EM model were used to prescribe the kinematics of the blood pool mesh which in turn was used for simulating hemodynamics in the CFD model. This was achieved by imposing $\mathbf{g}_{\mathrm{mov}} = \frac{\partial}{\partial t}\mathbf{d}_{\mathrm{s}}$ in Equation (37). Since the surface of the reference CFD blood pool mesh, $\partial\Omega_{\mathrm{f}}^0$, is not conformal with the surface of the reference EM blood pool mesh, $\Omega_{\mathrm{s,bp}}^0$, and the overlap of the two surfaces is imperfect due to smoothing of $\partial\Omega_{\mathrm{f}}^0$ and remeshing of Ω_{f}^0, a direct transfer of displacements between the two surfaces is not readily feasible. As a remedy, we proceeded as follows. After solving the EM problem the subset of displacements $\widetilde{\mathbf{d}}_{\mathrm{s}}$ that form the endocardial interface with the blood pool, $\Gamma_{\mathrm{s,bp}}^0$, were extracted from the solution $\mathbf{d}_{\mathrm{s}}$ defined at Ω_{s}^0. Since the mesh interface between Ω_{s}^0 and $\Omega_{\mathrm{s,bp}}^0$ is conformal the extracted displacements can be applied as inhomogeneous time-varying Dirichlet boundary conditions to the blood pool mesh $\Omega_{\mathrm{s,bp}}^0$ to solve a linear elastic problem given as

$$-\nabla_{\mathbf{X}} \cdot \boldsymbol{\sigma}(\mathbf{d}_{\mathrm{s}}(t)) = \mathbf{0} \qquad \text{in } \Omega_{s,\mathrm{bp}}^0, \tag{50}$$

$$\mathbf{d}_{\mathrm{s}}(t) = \widetilde{\mathbf{d}}_{\mathrm{s}}(t) \qquad \text{on } \partial\Omega_{s,\mathrm{bp}}^0, \tag{51}$$

where stress and strain tensor are

$$\boldsymbol{\sigma}(\mathbf{d}_{\mathrm{s}}) := \frac{E}{1+\nu} \left(\frac{\nu}{1-2\nu} \nabla_{\mathbf{X}} \cdot \mathbf{d}_{\mathrm{s}} \mathbf{I} + \boldsymbol{\varepsilon}(\mathbf{d}_{\mathrm{s}}) \right), \tag{52}$$

$$\boldsymbol{\varepsilon}(\mathbf{d}_{\mathrm{s}}) := \frac{1}{2} \left(\nabla_{\mathbf{X}} \mathbf{d}_{\mathrm{s}} + (\nabla_{\mathbf{X}} \mathbf{d}_{\mathrm{s}})^{\top} \right), \tag{53}$$

the constant E is Young's modulus in kPa and the constant ν is Poisson's ratio which is dimensionless in the range of $[-1, 0.5)$. Combining the solutions $\mathbf{d}_{\mathrm{s}}$ computed for Ω_{s}^0 and $\Omega_{\mathrm{s,bp}}^0$ yields displacements $\mathbf{d}_{\mathrm{s}}$ for $\Omega_{\mathrm{s,total}}^0$. Since $\partial\Omega_{\mathrm{f}}^0$ is fully embedded in this domain, $\Omega_{\mathrm{s,total}}^0$ $\Omega_{\mathrm{s,total}}^0$ can be used as a hanging background mesh for interpolating displacements onto the blood pool mesh, Ω_{f}^0, used for CFD simulations. However, for reasons of mesh quality, interpolation is solely applied on the boundary Ω_{f}^0 itself, and to find the interior displacement field the exact same linear elastic problem (50)–(53), is solved for $\mathbf{d}_{\mathrm{f}}$ instead of $\mathbf{d}_{\mathrm{s}}$. In both patient cases studied, ejection fractions were large leading to a substantial deformation of the blood pool mesh Ω_{f}^t. To maintain mesh quality under such large deformations the parameters E and ν governing stiffness and incompressibility of the material were altered accordingly. Initially, a fixed E_0 and ν_0 was chosen while the subsequent modification of E and ν was guided by a combination of the two following strategies.

i) *Quality based stiffening:* For each element τ_ℓ in the fluid mesh a tetrahedral quality indicator $\kappa(\tau_\ell)$ based on the movement from the previous time step was calculated, see [33, 45], and rescaled such that for elements of good quality κ is close to 1, while for elements with poor quality κ tends towards infinity. Eventually, the parameter E was multiplied by κ within each element.

ii) *ν-Volume based stiffening:* For larger deformation elements in the fluid mesh may collapse or even invert, yielding a zero or negative volume. When solving Equations (50)–(53), the current element volumes were tracked and a volume ratio relative to an undeformed reference element was computed as $\frac{|\tau_\ell|}{|\hat{\tau}_\ell|}$. For ratios below a predefined critical value the parameter ν was set close to 0.5 to make this element nearly incompressible.

2.4 Numerical Solution

Spatio-temporal discretization of all PDEs and the solution of the arising systems of equations relied upon the Cardiac Arrhythmia Research Package (CARP), see Vigmond et al. [84]. Numerical details on FE discretization [67] and solution of EP [85, 57, 58] and EM [6] have been discussed in detail elsewhere. FE discretization and solution of the Navier–Stokes equations were implemented recently using the same numerical framework which was extended to account for non-linear saddle-point problems arising from the discretized CFD equations.

Two time discretization schemes were implemented and compared for the applications in mind, and a computationally cheap semi-implicit scheme, modified from [30, Section 1.4.2], showed similar results to the more expensive fully-implicit generalized-α method [44]. Hence, all results in Section 3 were obtained using the semi-implicit scheme; to advance from time step t^n to t^{n+1}, only a linear block system needs to be solved, where each block depends on data from the previous time step only. Solvers for the block system were taken from the PETSc library [8, 9, 7]. We used a right preconditoned flexible GMRES method with PETSc fieldsplit preconditioning [73, 27] which in turn uses BoomerAMG [89] to approximate sub-block inverses. While the time step size for mechanics and CFD was the same, $\Delta t_{\text{mech}} = \Delta t_{\text{CFD}} = 0.5\,\text{ms}$, it was significantly smaller for EP, where $\Delta t_{\text{EP}} = 25\,\mu\text{s}$.

The implementation of the CFD solvers has been subjected to various validation procedures against standard CFD benchmarks [68]. All simulations were executed at the national HPC computing facility ARCHER in the United Kingdom using 384 and 768 cores for EM and CFD simulations, respectively.

2.5 Model parameterization

2.5.1 Electrophysiology

Electrical activation sequences were indirectly parameterized using the QRS complex of a given patient's ECG as guidance. Unlike in previous studies [5], we refrained from a detailed parameterization which aimed at reproducing the QRS complex of the ECG for a given patient by finding appropriate locations and timings for the main fascicles of the cardiac conduction system in the LV. Rather, default locations and timings were used which yielded a total activation time within the physiological range.

2.5.2 Passive biomechanics

The LV myocardium was characterized as a hyperelastic, nearly incompressible, transversely isotropic material with a nonlinear stressâĂŞstrain relationship [38]. Orthotropic material axes were aligned with the local fiber, sheet and sheet normal directions. To remove rigid body motion, homogeneous displacement boundary conditions were applied by fixing the terminal rims of the clipped brachiocephalic, left common carotid and left subclavian arteries as well as the clipped rim of the aorta descendens, see Figure 1. The model was stabilized by resting the LV apex on an elastic cushion of which the bottom face was rigidly anchored also by applying homogeneous displacement boundary conditions.

The constitutive model was fitted to recorded clinical data as previously reported with minor modifications [5]. The passive biomechanical model governed by the strain-energy function given in Equation (16) was fitted to approximate the end-diastolic pressure-volume relation (EDPVR). Due to limitations in the recorded data we refrained from directly fitting the model to the recorded pressure and volume data. Rather, only one data pair – EDV and end-diastolic pressure (EDP) – was used to fit the stress-free residual volume to the empiric Klotz relation [47] by adjusting the isotropic scaling parameter C_{Guc} in Equation (16). As the model anatomy was built from a segmented 3DWH MRI scan – acquired during diastasis – the FE model was inflated to increase the volume of the cavity by the difference between the volume at mid diastasis and the EDV. Using the end-diastolic geometry, default material parameters and the recorded EDP, an initial guess of the stress-free reference configuration was computed by unloading the model using a

backward displacement method [70, 15, 48]. The unloading procedure was repeated with varying trial material parameters, C_{Guc}, until the difference between the unstressed LV volume of the model and the prediction of the Klotz relation was less than 5 %.

2.5.3 Active stresses

Parameters of the active stress model were fitted during IVC and ejection phase. During IVC the LV volume was held constant [39] and the parameters of the active stress given in Equation (19) rate of contraction, τ_{c}, and peak active stress, S_{peak}, were manually adjusted to fit the maximum rate of rise of pressure, $(\mathrm{d}P/\mathrm{d}t)_{\mathrm{max}}$, and peak pressure, p_{lv}.

2.5.4 Afterload

When the LV pressure p_{lv} exceeded the aortic pressure, p_{ao}, ejection was initiated by connecting the LV model with the lumped 3-element Windkessel model [88]. Volume traces recorded from a given patient during ejection were used as input to compute aortic pressure traces by solving Equation (22). Both types of data were not recorded simultaneously as volume traces were computed from Cine MRI scans and pressure traces were recorded later invasively by catheterization. Volume and pressure traces were synchronized in time by aligning the onset of ejection of the volume trace $V_{\mathrm{lv}}(t)$ with the instant of opening of the aortic valve in the pressure trace $p_{\mathrm{ao}}(t)$. In those cases where heart rates were markedly different between the two measurements, volume traces were scaled in time to adjust LV ejection time (LVET) to the duration of ejection in the pressure traces, that is, the time elapsed between opening and closing of the aortic valve as these two instants in time were clearly identifiable in all traces $p_{\mathrm{ao}}(t)$, see Figure 3. Moreover, volume traces were offset to ensure that the model volume based on the segmentation of the 3DWH scan acquired during diastasis matched up with the Cine-MRI based volume trace at mid diastasis. The parameter space of the Windkessel model comprising characteristic impedance of the aorta, Z_{c}, as well as resistance, R, and compliance, C, of the arterial system was sampled using a recently developed stochastic sampling approach [21].

Numerous box constraints were used to constrain the search space of parameter sweeps. In particular, we used reported measurements in humans to define the mean values and restricted the search space for each parameter to fall within $\pm 20\,\%$ around the mean. Due to high frequency errors introduced by the pressure transducer we refrained from computing norms $||p_{\mathrm{ao,meas}} - p_{\mathrm{ao,fit}}||$ to quantify the deviations of fitted from measured pressure and opted for manual selection using three criteria, aortic peak pressure, p_{ao}, closing pressure of aortic valve and exponential decay of p_{ao} during diastole. For the sake of fitting Z_{c} we assumed $p_{\mathrm{ao}} \approx p_{\mathrm{lv}}$ since transvalvular pressure gradients in all patients were very minor.

2.5.5 CFD boundary conditions

The validated EM models yield the time-dependent displacement fields, $\mathbf{d}_{\mathrm{s}}$, which were transferred onto the fluid domain to drive simulations of blood flow in LV and aorta as described in Section 2.3.3 yielding $\mathbf{d}_{\mathrm{f}}(t, \mathbf{x})$ defined on the whole CFD mesh. Figure 4 (G) shows a summary of the boundary conditions. On the boundary $\Gamma^t_{\mathrm{f,mov}}$ a Dirichlet boundary condition enforcing the mesh velocity $\mathbf{w}^{\mathrm{h}}_{\mathrm{f}}$ is applied. On each aortic outlet $\Gamma_{\mathrm{f,outflow},i}(t)$ a 3-Element Windkessel model as described in Section 2.2.3 is attached. Further, the stabilization parameter β in Equation (38) was set to 0.2. Estimation of the input parameters for the hemodynamical Windkessel equations relied on an extension of the simple hydraulic analog of Ohm's law. Given the patient specific MAP, CO, and a percentage α_i of total CO running through the outlet the resistance R_i was estimated as

$$R_i \approx \frac{\mathrm{MAP}}{\alpha_i \mathrm{CO}}. \tag{54}$$

The percentages α_i were obtained either by measurement or by applying Murray's law [56]. The impedances Z_i were chosen as 5 % of R_i, and the compliances C_i were chosen such that $R_i C_i \approx$

1000 ms. To keep the semi-implicit character of the CFD system the Windkessel equations were solved with a semi-implicit backward Euler method using the flow q_i^n through the aortic outlet, from the previous time step as input.

3 Results

3.1 Building electromechanical kinematic driver models

Using a previously developed automated workflow [20], anatomical FE models of LV and aorta were built for patient cases *28-Pre* and *44-Pre* based on segmented imaging data acquired under pre-treatment conditions. Figure 1 illustrates the key processing steps and the resulting FE model for case *28-Pre*. For the case *28-Pre* the CoA was repaired by a virtual dilatation procedure applied to the segmented image data with the aim to restore normal cross sectional areas. Subsequently, a new FE mesh was generated referred to as *28-Post*, which was essentially identical to *28-Pre*, with the only difference being the anatomical adjustment of the CoA in the aortic arch to the target post-treatment anatomy after stenting, see Figure 5.

Passive biomechanical properties, afterload and active stress models of cases *28-Pre* and *44-Pre* were parameterized using clinically recorded pressure and volume data under pre-treatment conditions, see Figure 3A. The fitted final parameters used are summarized in Table 3. The goodness of fit of both integrated EM models was verified by standard PV loop analysis as shown in Figure 3B. Results of a quantitative comparison with clinically derived metrics including EF, EDV and ESV, CO, and peak systolic pressure are summarized in Table 5.

3.2 Blood pool FE modeling for CFD

Conformal FE blood pool meshes were extracted from EM FE meshes, surfaces were smoothed and used for volumetric remeshing with increased spatial resolution including boundary layers. The corresponding workflow is illustrated in Figure 4.

Kinematics of the EM model were transferred to the CFD blood pool mesh and the result is illustrated in terms of displacements $\mathbf{d}_\mathrm{s}, \mathbf{d}_\mathrm{f}$ in Panel (II) of Figure 6. Due to the large EF of about 65 % for both *28-Pre* and *44-Pre*, the blood pool underwent a significant deformation. However, using a combination of element quality and ν-Volume based stiffening with an initial Young's Modulus $E_0 = 100\,\mathrm{kPa}$ and Poisson's ratio $\nu_0 = 0.3$, sufficient element quality was preserved throughout the entire ejection phase and numerical instabilities could be avoided. Panel (I) of Figure 6 shows the 80^{th}-percentile of bad element quality against the number of linear iterations required for convergence for the *28-Pre* case. The quality of elements was calculated with the same quality inidcator [33, 45] as described in Section 2.3.3 but was rescaled to the interval $[0, 1]$, with the best element quality being 0 and the worst element quality being 1. The modest increase in iteration numbers of the iterative preconditioned GMRES solver provides indirect evidence of sufficiently preserved mesh quality (see Figure 6). Spatially, most lower quality elements were located in the CFD boundary layer.

3.3 Numerical CFD benchmarks

The implementation of the Navier–Stokes solver was verified by solving a set of standardized benchmark problems, see [68]. Computational performance was evaluated by performing strong scaling experiments by repeating the post-treatment hemodynamics simulation of case *28-Post* with varying numbers of cores ranging from 96 to 1536. Details on computational complexity and costs are summarized in Table 6. For temporal discretization a time step of $\Delta t = 0.5\,\mathrm{ms}$ was used to simulate the ejection phase lasting for 208 ms. The overall discrete system comprised 5 177 056 degrees of freedom, which was solved over 416 time steps. Strong scaling results are summarized in Figure 7. Efficient strong scaling behavior was observed up to 768 cores with parallel efficiency slowly degrading from 100 % at 96 cores down to 55 % at 768 cores. Scalability stalled when doubling the core count to 1536 which reduced the degrees of freedom per parallel partition down

to 3386. Parallel efficiency dropped to 27 % which is attributed due to the unfavorable ratio between local compute work and communication.

3.4 Simulating cardiac and cardiovascular hemodynamics

Hemodynamics in the LV and aorta was simulated using the EM simulations as a kinematic driver. Flow rates through various aortic cross sections and outflow orifices were calculated as the integral over measured fluxes through the cross-sectional plane for both 4D VEC MRI and simulated flow data. At locations of interest which were $\varepsilon_{\mathrm{DSC}}$, $\varepsilon_{\mathrm{BCA}}$, $\varepsilon_{\mathrm{LCA}}$ and $\varepsilon_{\mathrm{LSCA}}$ denoting cross sections in the aorta descendens and the orifices of brachocephalic, left carotid and left subclavian artery, respectively, relative flows were computed from 4D VEC MRI data as fractions α_i expressed in percent of the total peak flow through the aorta ascendens as determined over the plane $\varepsilon_{\mathrm{ASC}}$. For those planes of interest where measurements were not feasible due to noise, flow percentages were estimated based on Murray's law. Flow curves during ejection at selected cross sections are shown in Subfigures (A), and (E) of Figure 8. MAP and computed mean flow through each outlet orifice were used to determine the parameters of the coupled Windkessel models of afterload in Equations (23, 24), see Tables 7 and 8. In the *28-Pre* case this resulted in flow splits of $\alpha_i \approx 23\,\%, 51.3\,\%, 12.83\,\%$ and $12.83\,\%$ whereas in the *44-Pre* case the flow split ratios were $\alpha_i \approx 5.68\,\%$, $57.45\,\%$ and $34.01\,\%$ for $\varepsilon_{\mathrm{DSC}}$, $\varepsilon_{\mathrm{BCA}}$, $\varepsilon_{\mathrm{LCA}}$ and $\varepsilon_{\mathrm{LSCA}}$, respectively.

For the CFD analysis a time step of $\Delta t = 0.5\,\mathrm{ms}$ was used. The ejection phases of the EM simulations were chosen as time horizons for the CFD simulation which lasted from $t = 90\,\mathrm{ms}$ to $t = 302\,\mathrm{ms}$ in the *28-Pre* case and from $t = 70\,\mathrm{ms}$ to $t = 329\,\mathrm{ms}$ in the *44-Pre* case, yielding 424 and 518 time steps, respectively. The Windkessel parameters for each outlet, calculated as described in Section 2.5.5, are summarized in Tables 7 and 8. Pressure p_{f} along the centerline s_{c} and fluxes through the planes $\varepsilon_{\mathrm{DSC}}$, $\varepsilon_{\mathrm{LSC}}$, $\varepsilon_{\mathrm{BCA}}$, and $\varepsilon_{\mathrm{ASC}}$ were computed at the instant of peak flow in the aorta ascendens and compared against measured data, which were pressures derived from Pressure–Poisson mapping (see Subfigure (D) of Figure 8) and 4D VEC MRI fluxes. For case *28-Pre* pressure drops were calculated from the pressure values on the intersection of the centerline and $\varepsilon_{\mathrm{DSC}}$, $\varepsilon_{\mathrm{ASC}}$ respectively. Further, we calculated the average pressure over the aforementioned planes as well. Both ways yielded a simulated pressure drop across the CoA of $\approx 29.2\,\mathrm{mmHg}$ which agreed well with the clinically estimated pressure drop of $\approx 30\,\mathrm{mmHg}$. Furthermore, we calculated the flux through the various planes and compared them against the clinically estimated fluxes. A quantitative comparison of fluxes is given in Table 9. Subfigures (C), (G), and (H) of Figure 8 show velocity profiles at peak flow condtions.

3.5 post-treatment simulations

Simulations of case *28-Pre* were repeated on geometry of case *28-Post* using almost the same set of parameters, see Table 3. Only S_{peak} was slightly adjusted, which resulted in a better peak pressure value in the LV. The geometry of case *28-Post* was almost identical to case *28-Pre* with the only exception being the virtual repair of CoA anatomy. In this scenario only pre- and post-treatment simulations were compared to evaluate their relative differences in terms of pressure and flow velocities. Figure 9 shows results. Pressure drops were calculated as in Subsection 3.4 for both scenarios. For *28-Pre* we calculated a pressure drop of $\approx 29.2\,\mathrm{mmHg}$ while for *28-Post* a pressure drop of $\approx 14.15\,\mathrm{mmHg}$ was calculated.

4 Discussion

In this study, we report on the progress made towards a novel EMF model of the human LV that is entirely based on first principles and as such, in principle, is able to represent all cause-effect relationships with full biophysical detail. Unlike in the majority of cardiac CFD studies where the use of image-based kinematic driver models prevails, EM LV and aorta models of CoA patients were employed to serve as a kinematic driver to a computational model of hemodynamics in the

LV cavity and aorta. A hybrid two stage modeling approach was adopted with regard to hemodynamics where EM and CFD model are executed sequentially. First, in the EM simulations the afterload imposed by the circulatory system upon the LV was represented by a lumped model to compute LV kinematics. These EM models were carefully fitted to available clinical data to replicate important clinical metrics characterizing hemodynamic and biomechanical work performed by the LV [37]. In a subsequent step, a full-blown ALE-based CFD model with moving domain boundaries was *unidirectionally* or *weakly* coupled to the EM model. The motion of the fluid domain was driven by the kinematics of the EM model. Kinematics was transferred from EM mesh onto the CFD blood pool mesh by generating a combined kinematic model comprising LV, valve, aortic structure and a conformal blood pool mesh which served as a hanging background mesh for interpolation. The higher resolution blood pool CFD mesh with refined boundary layers was fully immersed in the EM background mesh. Kinematics was transferred by interpolation only onto the surface of the CFD blood pool mesh and extended into the volume of the blood pool by solving a linear solid mechanics problem.

We show validation results for two selected clinical CoA cases under pre-treatment conditions and compare between pre-treatment and post-treatment for one patient case in which the CoA was anatomically modified by a virtual stenting procedure. Further, we demonstrate numerical tractability of the implemented approach by providing strong scaling benchmark results. The overall cost of the entire work flow for building, fitting and execution of EMF simulations is comparable to plain image-based kinematic driver models [55], suggesting that the proposed methodology may be, in principle, compatible with clinical time scales.

4.1 Biomechanical modeling versus image-based kinematics

Modalities such as CMR and Cardiac CT on the other hand, provide excellent spatial resolution. CMR has an in-plane resolution of $1.5 \times 1.5\,\text{mm}$, but more limited through-plane resolution (typically about 8 mm) while CT is capable of isotropic spatial resolution on the sub millimeter scale ($\approx 0.5\,\text{mm}$) and clear delineation of trabeculae and lumen boundaries. CMR has the advantage of higher temporal resolution (30 to 50 ms) while temporal resolution in CT depends on the scanning system (50 to 200 ms). This is orders-of-magnitude lower than the temporal resolution required for the flow simulation (≈ 1000 phases per cardiac cycle) and appropriate interpolation methods need to be employed to create CFD-ready models. This stage of model generation has been very difficult to automate, and remains the biggest bottleneck for patient-specific cardiac flow modeling. Compared to pure image-based kinematic approaches our model is able to compute, e.g., the spatio-temporal distribution of wall stresses, power density, the length of diastolic intervals available for myocardial perfusion, O_2 consumption, and metabolic supply/demand ratios. The variations of all these parameters in response to a changed afterload and many other biomarkers of physiological interest can be derived, which is not feasible with image-based models.

4.2 Kinematic transfer to CFD blood pool model

Both patients modeled in this study featured healthy EFs of $> 60\,\%$, that is, EF was $\approx 65\,\%$ in both cases. At a such high EFs the wall motion of the LV is significant, leading to substantial reductions in the LV blood pool volume. IB methods [19, 71, 86] are known to be more convenient to cope with the large deformation of the CFD blood pool [65]. IB methods and other non-boundary-fitting methods rely on a fixed fluid mesh and the moving wall of the ventricle is not explicitly tracked. The coupling between the CFD mesh and the structure is performed via Dirac Delta functions (IB) or Lagrange multipliers (fictitious domain methods) and is usually realized by introducing additional degrees of freedom on interface cut elements. While mesh generation is only necessary prior to computation fixed mesh methods typically require adaptive mesh refinement or modifications [87] to obtain reasonable accuracy for the solution near the fluid-solid interface.

In contrast, ALE algorithms capture the fluid-solid interface more accurately, are in general stable and easy to implement, no extra degrees of freedoms are introduced, and computational costs are low in comparison [82, 77]. However, it is often assumed that unstructured FE approaches, as

implemented in this paper, critically depend on automatic remeshing strategies [51] to keep mesh quality within acceptable bounds [55]. Our study demonstrates that this may not necessarily be the case. While the mesh quality decreased with deformation over the course of ejection, the linear elastic deformation of the CFD blood pool mesh combined with the quality-based stiffening approach prevented the degeneration of any elements. The number of elements in which element quality degraded noticeably was very small. As illustrated in Figure 6, virtually all elements of reduced quality were located in the higher resolution boundary layer of the CFD blood pool mesh. According to the element quality metric used, an element quality of 1 refers to a fully degenerated element of zero volume. Despite the significant compression of the blood pool mesh, not a single element was deformed to this degree. Even when applying a stricter threshold where element quality is deemed poor if the quality indicator is > 0.8, which is not critical from a numerical point of view, the number of elements in this range remained small with $< 0.8\,\%$ (Figure 6). The worst element quality observed in the entire mesh was 0.9994. Using a threshold of > 0.95 where element quality may be sufficiently poor to impact more notably on solver performance, only 24 out of 2506987 elements were found. Nonetheless, an increase in number of linear iterations required for convergence was observed which is likely to be linked to the gradual degradation of element quality. The number of iterations per solver step increased from around ≈ 17 iterations during early ejection up to ≈ 80 iterations during late ejection. While the more than fourfold increase in linear iterations negatively impacted overall solver performance and rendered simulations computationally more expensive, the complexity of automatic remeshing was avoided. We consider this a pivotal importance as automatic remeshing in combination with a MPI parallel FE solver is definitely feasible, but highly non-trivial to implement robustly and efficiently.

4.3 Computational feasibility

Computational feasibility of human scale cardiac simulations by using strongly scalable numerical implementations has been demonstrated previously for electrophysiology [60] and mechanics [6]. More recently, we reported on a novel reaction-eikonal model which reduces the cost of EM simulations significantly by alleviating constraints imposed by reaction-diffusion models upon mesh resolution [58]. In this study, this recent reaction-eikonal approach was used for simulating EM using the same FE grid with an average resolution of ≈ 1 mm for both EP and mechanics. Such lower resolutions suffice for solving for mechanics with sufficient accuracy [50]. The overall reduction in terms of nodes and degrees of freedom reduces the compute cost substantially, rendering simulations in desktop environments feasible. Using 96 cores, EM simulations of a full cardiac cycle only lasted ≈ 180 min which facilitated sufficiently short simulation cycles for efficient model fitting. The entire workflow for building and parameterizing one patient-specific EM model is feasible within a day.

Owing to the higher resolution of the blood pool mesh and the presences of a refined boundary layer the number of nodes and degrees of freedom were higher than for EM simulations, around 350000/1500000 nodes/degrees of freedom for case *28-Pre* and 400000/1700000 nodes/degrees of freedom for case *44-Pre*, respectively. To assess strong scaling properties of our CFD solver implementation, the resolution was further increased to 1300000/5000000 nodes/degrees of freedom for case *28-Post* to cover a wider range of core counts. Strong scaling efficiency leveled off when doubling from 768 to 1536 cores. Local compute load with 1536 was 900/2600 nodes/degrees of freedom per core. The patient simulations were performed using 384 cores, resulting in a load per core of about 900/2700 nodes/dofs, respectively. At these resolutions CFD simulations were executed in ≈ 40 min, suggesting that compatibility with clinical time frames will be achievable.

4.4 Limitations

In the presented modeling approach numerous simplifying assumptions were made which may affect the biophysical fidelity of the model. In particular, while the aorta was taken into account as a solid structure in the EM simulations, its biomechanical description was simplified by assuming

isotropic behavior, that is, the fibrous organization of aortic walls remained unaccounted for [4]. Further, as our main focus was on the EM of the LV and, to a much lesser degree, on the aorta, the aortic lumen remained unpressurized and, in absence of distensibility measurements of the aortic wall, parameters of the passive biomechanics model used for the aortic wall were not fitted. Thus the model of the aorta does not respond to the rise in pressure during ejection with an adequate distension ΔV of its lumen. In the CFD simulations $\Delta V \approx 0$ translates into a stiff aorta of low compliance which may cause a bias towards overestimation of the computed pressure fields. Further, the influence of the aortic valve upon blood flow was not taken into account. Rather, it was assumed that with the start of ejection the aortic valve is in its full open configuration, which allows blood flow over the entire orifice area and in which the valve does not influence the blood flow out of the LV in a significant way. Since only CoA patients were modeled which showed no indications of AVD this simplifying assumption may be well justified.

A potential main strength of the presented modeling approach – the ability to predict the biomechanical response of the LV to changed flow patterns in the aorta – was not exploited. Due to the weak FSI coupling the immediate feedback of altered flow or changed pressure gradients in the aorta on LV biomechanics was ignored. In our current modeling approach any such feedback must be mediated through changes in the parameterization of the lumped afterload model. However, owing to regulatory mechanism of the circulatory system level this is not directly predictable with the modeling setup used in this study as flow distribution through the four outlets will be influenced by factors which cannot be accounted for in a model comprising only LV, aorta and lumped outflow impedances. In any case, one cannot assume that the computed changes in pressure gradients across a CoA translate directly into a reduction in LV peak pressure. Independently of the modeling approach taken – be it a strongly or weakly coupled FSI model – a lumped model of systemic regulation is likely to be necessary to predict altered LV loading under post-treatment conditions [3, 52]. Compared to a fully coupled FSI model our approach is limited in the sense that CFD simulations do not influence the behavior of the EM model. However, in many clinical settings CFD simulations in the aortic arch and LV with image based kinematics prevail. Image based kinematic models can only depict the *status quo* of a patient. With our personalized EM model, based on first principles, we can do simulations altering the motion, simply by changing input paramters. The altered motion is then reflected in the CFD simulation. Examples would include changes in heart beats, infarcts or LBBB conditions. In this work, the effect of stenting was only accounted for by a geometric change in the computational geometry and an ad hoc adjustement of the lumped model parameters. In future studies, we intend to use a 1-D model of the arterial tree coupled to a 0-D lumped model at the aortic outlets, thus being able to account for the effect of stenting in a more detailed fashion, see for example [65]. As a first step towards our ultimate goal of a fully coupled FSI model, that is based entirely on first principles, we will add the dynamic fluid pressure $\frac{\rho_\mathrm{f}}{2}\left|\mathbf{u}_\mathrm{f}\right|^2$ to the pressure of the lumped model (0-D or 1-D). This results in a spatio-temporal pressure inside the LV and the aorta, and to incorporate the dynamic feedback of fluid upon structure we will iterate between a CFD solving step and a EM solving step within each timestep to guarantee a converged solution.

5 Conclusion

Biophysically detailed models of LV EM can be efficiently built and parameterized with clinical data to be considered a viable option for patient-specific simulation. Similar to image-based kinematic models such biophysics-based EM models can be used as a kinematic driver for simulating cardiac and vascular hemodynamics. The cost of model building and execution is comparable between the two approaches. Biophysical EM models offer the significant advantage of being based entirely on first principles and as such, may allow to make predictions of interventions altering pressure and flow patterns onto LV performance. In contrast, image-based kinematics modeling may provide a more accurate representation of blood pool motion, at least under pre-treatment conditions or post-treatment conditions secondary to interventions which do not influence LV kinematics in a significant way.

Conflict of Interest Statement

The authors declare that the research was conducted in the absence of any commercial or financial relationships that could be construed as a potential conflict of interest.

Author Contributions

EK, GP contributed conception and design of the study; LG, TK acquired and processed clinical data; EK, MG, AN and CA developed numerical methodology; AJP contributed by conceiving modeling workflows and FE meshing; LM and MG developed parameterization of electromechanical model; EK, MG, CA and GP analyzed and interpreted simulation data; EK, CA and GP drafted the article; EK, CA, MG, LG and GP critically revised the article; All authors contributed to manuscript revision, read, and approved the submitted version.

Funding

This research was supported by the grants F3210-N18 and I2760-B30 from the Austrian Science Fund (FWF), the EU grant CardioProof agreement 611232 and a BioTechMed award to GP, and a Marie Skłodowska–Curie fellowship (GA 750835) to CA. We acknowledge PRACE for awarding us access to resource ARCHER based in the UK at EPCC (grant CAMEL) and the Vienna Scientific Cluster VSC-3.

References

[1] Magnus Andersson, Jonas Lantz, Tino Ebbers, and Matts Karlsson. Multidirectional WSS disturbances in stenotic turbulent flows: A pre-and post-intervention study in an aortic coarctation. *Journal of Biomechanics*, 51:8–16, 2017.

[2] Luca Antiga, Marina Piccinelli, Lorenzo Botti, Bogdan Ene-Iordache, Andrea Remuzzi, and David A Steinman. An image-based modeling framework for patient-specific computational hemodynamics. *Medical & Biological Engineering & Computing*, 46(11):1097, 2008.

[3] Theo Arts, Tammo Delhaas, Peter Bovendeerd, Xander Verbeek, and Frits Prinzen. Adaptation to mechanical load determines shape and properties of heart and circulation: the CircAdapt model. *Am. J. Physiol. Heart Circ. Physiol.*, 288:1943–1954, 2005.

[4] Christoph M. Augustin, Gerhard A. Holzapfel, and Olaf Steinbach. Classical and all-floating FETI methods for the simulation of arterial tissues. *International Journal for Numerical Methods in Engineering*, 99(4):290–312, 2014.

[5] Christoph M. Augustin, Andrew Crozier, Aurel Neic, Anton J. Prassl, Elias Karabelas, Tiago Ferreira da Silva, Joao F. Fernandes, Fernando Campos, Titus Kuehne, and Gernot Plank. Patient-specific modeling of left ventricular electromechanics as a driver for haemodynamic analysis. *EP Europace*, 18(Supplement 4):iv121–iv129, 2016.

[6] Christoph M Augustin, Aurel Neic, Manfred Liebmann, Anton J Prassl, Steven A Niederer, Gundolf Haase, and Gernot Plank. Anatomically accurate high resolution modeling of human whole heart electromechanics: A strongly scalable algebraic multigrid solver method for nonlinear deformation. *Journal of Computational Physics*, 305:622–646, 2016.

[7] Satish Balay, William D. Gropp, Lois Curfman McInnes, and Barry F. Smith. Efficient management of parallelism in object oriented numerical software libraries. In E. Arge, A. M. Bruaset, and H. P. Langtangen, editors, *Modern Software Tools in Scientific Computing*, pages 163–202. Birkhäuser Press, 1997.

[8] Satish Balay, Shrirang Abhyankar, Mark F. Adams, Jed Brown, Peter Brune, Kris Buschelman, Lisandro Dalcin, Victor Eijkhout, William D. Gropp, Dinesh Kaushik, Matthew G. Knepley, Lois Curfman McInnes, Karl Rupp, Barry F. Smith, Stefano Zampini, Hong Zhang, and Hong Zhang. PETSc Web page. `http://www.mcs.anl.gov/petsc`, 2016.

[9] Satish Balay, Shrirang Abhyankar, Mark F. Adams, Jed Brown, Peter Brune, Kris Buschelman, Lisandro Dalcin, Victor Eijkhout, William D. Gropp, Dinesh Kaushik, Matthew G. Knepley, Lois Curfman McInnes, Karl Rupp, Barry F. Smith, Stefano Zampini, Hong Zhang, and Hong Zhang. PETSc users manual. Technical Report ANL-95/11 - Revision 3.7, Argonne National Laboratory, 2016.

[10] J. D. Bayer, R. C. Blake, G. Plank, and N. A. Trayanova. A novel rule-based algorithm for assigning myocardial fiber orientation to computational heart models. *Annals of Biomedical Engineering*, 40(10):2243–2254, 2012.

[11] Y Bazilevs, VM Calo, JA Cottrell, TJR Hughes, A Reali, and G Scovazzi. Variational multiscale residual-based turbulence modeling for large eddy simulation of incompressible flows. *Computer Methods in Applied Mechanics and Engineering*, 197(1):173–201, 2007.

[12] Yuri Bazilevs, Kenji Takizawa, and Tayfun E Tezduyar. *Computational fluid-structure interaction: methods and applications*. John Wiley & Sons, 2013.

[13] CristÃşbal Bertoglio, Alfonso Caiazzo, Yuri Bazilevs, Malte Braack, Mahdi Esmaily, Volker Gravemeier, Alison L. Marsden, Olivier Pironneau, Irene E. Vignon-Clementel, and Wolfgang A. Wall. Benchmark problems for numerical treatment of backflow at open boundaries. *International Journal for Numerical Methods in Biomedical Engineering*, page e2918, 2017.

[14] Pavel B Bochev, Clark R Dohrmann, and Max D Gunzburger. Stabilization of low-order mixed finite elements for the stokes equations. *SIAM Journal on Numerical Analysis*, 44(1): 82–101, 2006.

[15] Joris Bols, Joris Degroote, Bram Trachet, Benedict Verhegghe, Patrick Segers, and Jan Vierendeels. A computational method to assess the in vivo stresses and unloaded configuration of patient-specific blood vessels. *Journal of Computational and Applied Mathematics*, 246:10–17, 2013.

[16] Malte Braack, Piotr Boguslaw Mucha, and Wojciech Zajaczkowski. Directional do-nothing condition for the Navier–Stokes equations. *Journal of Computational Mathematics*, 32(5): 507–521, 2014.

[17] Susanne Brenner and Ridgway Scott. *The mathematical theory of finite element methods*, volume 15. Springer Science & Business Media, 2007.

[18] C. Chnafa, S. Mendez, and F. Nicoud. Image-based large-eddy simulation in a realistic left heart. *Comput. Fluids*, 94:173–187, 2014. ISSN 00457930.

[19] Young Joon Choi, Jason Constantino, Vijay Vedula, Natalia Trayanova, and Rajat Mittal. A new MRI-based model of heart function with coupled hemodynamics and application to normal and diseased canine left ventricles. *Frontiers in Bioengineering and Biotechnology*, 3: 140, 2015.

[20] A Crozier, C M Augustin, A Neic, A J Prassl, M Holler, T E Fastl, A Hennemuth, K Bredies, T Kuehne, M J Bishop, S A Niederer, and G Plank. Image-based personalization of cardiac anatomy for coupled electromechanical modeling. *Annals of Biomedical Engineering*, 44: 58–70, 2016.

[21] Andrew Crozier, Bojan Blazevic, Pablo Lamata, Gernot Plank, Matthew Ginks, Simon Duckett, Manav Sohal, Anoop Shetty, Christopher A Rinaldi, Reza Razavi, et al. The relative role of patient physiology and device optimisation in cardiac resynchronisation therapy: A computational modelling study. *Journal of Molecular and Cellular Cardiology*, 96:93–100, 2016.

[22] A. de Vecchi, A. Gomez, K. Pushparajah, T. Schaeffter, J.M. Simpson, R. Razavi, G.P. Penney, N.P. Smith, and D.A. Nordsletten. A novel methodology for personalized simulations of ventricular hemodynamics from noninvasive imaging data. *Computerized Medical Imaging and Graphics*, 51(Supplement C):20 – 31, 2016.

[23] Hilmi Demiray. A note on the elasticity of soft biological tissues. *Journal of Biomechanics*, 5(3):309–311, 1972.

[24] Torsten Doenst, Kathrin Spiegel, Michael Reik, Michael Markl, Jürgen Hennig, Stefan Nitzsche, Friedhelm Beyersdorf, and Herbert Oertel. Fluid-dynamic modeling of the human left ventricle: methodology and application to surgical ventricular reconstruction. *The Annals of Thoracic Surgery*, 87(4):1187–1195, 2009.

[25] Jean Donea and Antonio Huerta. *Finite element methods for flow problems*. John Wiley & Sons, 2003.

[26] Jim Douglas and Jun Ping Wang. An absolutely stabilized finite element method for the stokes problem. *Mathematics of Computation*, 52(186):495–508, 1989.

[27] Howard Elman, Victoria E Howle, John Shadid, Robert Shuttleworth, and Ray Tuminaro. A taxonomy and comparison of parallel block multi-level preconditioners for the incompressible Navier–Stokes equations. *Journal of Computational Physics*, 227(3):1790–1808, 2008.

[28] Mahdi Esmaily Moghadam, Yuri Bazilevs, Tain-Yen Hsia, Irene E. Vignon-Clementel, and Alison L. Marsden. A comparison of outlet boundary treatments for prevention of backflow divergence with relevance to blood flow simulations. *Computational Mechanics*, 48(3):277–291, 2011.

[29] Ch Förster, Wolfgang A Wall, and Ekkehard Ramm. On the geometric conservation law in transient flow calculations on deforming domains. *International Journal for Numerical Methods in Fluids*, 50(12):1369–1379, 2006.

[30] Davide Forti. *Parallel Algorithms for the Solution of Large-Scale Fluid-Structure Interaction Problems in Hemodynamics*. PhD thesis, SB, Lausanne, 2016.

[31] Justine Fouchet-Incaux. Artificial boundaries and formulations for the incompressible Navier–Stokes equations: applications to air and blood flows. *SeMA Journal*, 64(1):1–40, 2014.

[32] Leopoldo P Franca and Thomas JR Hughes. Two classes of mixed finite element methods. *Computer Methods in Applied Mechanics and Engineering*, 69(1):89–129, 1988.

[33] Lori A Freitag and Patrick M Knupp. Tetrahedral mesh improvement via optimization of the element condition number. *International Journal for Numerical Methods in Engineering*, 53 (6):1377–1391, 2002.

[34] L Goubergrits, R Mevert, P Yevtushenko, J Schaller, U Kertzscher, S Meier, S Schubert, E Riesenkampff, and T Kuehne. The impact of MRI-based inflow for the hemodynamic evaluation of aortic coarctation. *Annals of Biomedical Engineering*, 41(12):2575–2587, 2013.

[35] Leonid Goubergrits, Eugenie Riesenkampff, Pavlo Yevtushenko, Jens Schaller, Ulrich Kertzscher, Anja Hennemuth, Felix Berger, Stephan Schubert, and Titus Kuehne. MRI-based computational fluid dynamics for diagnosis and treatment prediction: Clinical validation study in patients with coarctation of aorta. *Journal of Magnetic Resonance Imaging*, 41 (4):909–916, 2015.

[36] Philip M Gresho and Robert L Sani. On pressure boundary conditions for the incompressible Navier–Stokes equations. *International Journal for Numerical Methods in Fluids*, 7(10):1111–1145, 1987.

[37] M A F Gsell, C M Augustin, A J Prassl, J F Fernandes, M Kelm, L Goubergrits, T Kuehne, and G Plank. Assessment of wall stresses and internal mechanical heart power in the left ventricle: Finite element modeling versus Laplace analysis. *International Journal for Numerical Methods in Biomedical Engineering*, 2018.

[38] Julius M. Guccione, Kevin D. Costa, and Andrew D. McCulloch. Finite element stress analysis of left ventricular mechanics in the beating dog heart. *Journal of Biomechanics*, 28(10):1167 – 1177, 1995.

[39] Viatcheslav Gurev, Pras Pathmanathan, Jean-Luc Fattebert, Hui-Fang Wen, John Magerlein, Richard A Gray, David F Richards, and J Jeremy Rice. A high-resolution computational model of the deforming human heart. *Biomechanics and Modeling in Mechanobiology*, 14: 829–849, 2015.

[40] Marc Hirschvogel, Marina Bassilious, Lasse Jagschies, Stephen M. Wildhirt, and Michael W. Gee. A monolithic 3D-0D coupled closed-loop model of the heart and the vascular system: Experiment-based parameter estimation for patient-specific cardiac mechanics. *International Journal for Numerical Methods in Biomedical Engineering*, 33(8):e2842, 2017.

[41] CW Hirt, Anthony A Amsden, and JL Cook. An arbitrary Lagrangian–Eulerian computing method for all flow speeds. *Journal of Computational Physics*, 14(3):227–253, 1974.

[42] Thomas JR Hughes. Multiscale phenomena: Green's functions, the Dirichlet-to-Neumann formulation, subgrid scale models, bubbles and the origins of stabilized methods. *Computer Methods in Applied Mechanics and Engineering*, 127(1-4):387–401, 1995.

[43] Thomas JR Hughes, Leopoldo P Franca, and Marc Balestra. A new finite element formulation for computational fluid dynamics: V. Circumventing the Babuška–Brezzi condition: a stable Petrov–Galerkin formulation of the Stokes problem accommodating equal-order interpolations. *Computer Methods in Applied Mechanics and Engineering*, 59(1):85–99, 1986.

[44] Kenneth E Jansen, Christian H Whiting, and Gregory M Hulbert. A generalized-α method for integrating the filtered Navier–Stokes equations with a stabilized finite element method. *Computer Methods in Applied Mechanics and Engineering*, 190(3):305–319, 2000.

[45] Harish Kanchi and Arif Masud. A 3D adaptive mesh moving scheme. *International Journal for Numerical Methods in Fluids*, 54(6-8):923–944, 2007.

[46] M Kelm, L Goubergrits, J Bruening, P Yevtushenko, JF Fernandes, SH Sündermann, F Berger, T Kuehne, S Nordmeyer, et al. Model-based therapy planning allows prediction of haemodynamic outcome after aortic valve replacement. *Scientific Reports*, 7:9897, 2017.

[47] Stefan Klotz, Marc L Dickstein, and Daniel Burkhoff. A computational method of prediction of the end-diastolic pressure–volume relationship by single beat. *Nature Protocols*, 2(9):2152–2158, 2007.

[48] Adarsh Krishnamurthy, Christopher T Villongco, Joyce Chuang, Lawrence R Frank, Vishal Nigam, Ernest Belezzuoli, Paul Stark, David E Krummen, Sanjiv Narayan, Jeffrey H Omens, et al. Patient-specific models of cardiac biomechanics. *Journal of Computational Physics*, 244:4–21, 2013.

[49] Sebastian B.S. Krittian, Pablo Lamata, Christian Michler, David A. Nordsletten, Jelena Bock, Chris P. Bradley, Alex Pitcher, Philip J. Kilner, Michael Markl, and Nic P. Smith. A finite-element approach to the direct computation of relative cardiovascular pressure from time-resolved MR velocity data. *Medical Image Analysis*, 16(5):1029 – 1037, 2012.

[50] Sander Land, Viatcheslav Gurev, Sander Arens, Christoph M Augustin, Lukas Baron, Robert Blake, Chris Bradley, Sebastian Castro, Andrew Crozier, Marco Favino, Thomas E Fastl, Thomas Fritz, Hao Gao, Alessio Gizzi, Boyce E Griffith, Daniel E Hurtado, Rolf Krause, Xiaoyu Luo, Martyn P Nash, Simone Pezzuto, Gernot Plank, Simone Rossi, Daniel Ruprecht, Gunnar Seemann, Nicolas P Smith, Joakim Sundnes, J Jeremy Rice, Natalia Trayanova, Dafang Wang, Zhinuo Jenny Wang, and Steven A Niederer. Verification of cardiac mechanics software: benchmark problems and solutions for testing active and passive material behaviour. *Proceedings. Mathematical, Physical, and Engineering Sciences*, 471:20150641, 2015.

[51] CC Long, AL Marsden, and Y Bazilevs. Fluid–structure interaction simulation of pulsatile ventricular assist devices. *Computational Mechanics*, 52(5):971–981, 2013.

[52] Joost Lumens, Tammo Delhaas, Borut Kirn, and Theo Arts. Three-wall segment (TriSeg) model describing mechanics and hemodynamics of ventricular interaction. *Ann. Biomed. Eng.*, 37(11):2234–55, 2009.

[53] S. Meier, A. Hennemuth, O. Friman, J. Bock, M. Markl, and T. Preusser. Non-invasive 4D blood flow and pressure quantification in central blood vessels via PC-MRI. In A. Murray, editor, *2010 Computing in Cardiology*, pages 903–906, 2010.

[54] Viorel Mihalef, Razvan Ioan Ionasec, Puneet Sharma, Bogdan Georgescu, Ingmar Voigt, Michael Suehling, and Dorin Comaniciu. Patient-specific modelling of whole heart anatomy, dynamics and haemodynamics from four-dimensional cardiac ct images. *Interface Focus*, 1 (3):286–296, 2011.

[55] Rajat Mittal, Jung Hee Seo, Vijay Vedula, Young J Choi, Hang Liu, H Howie Huang, Saurabh Jain, Laurent Younes, Theodore Abraham, and Richard T George. Computational modeling of cardiac hemodynamics: current status and future outlook. *Journal of Computational Physics*, 305:1065–1082, 2016.

[56] Cecil D Murray. The physiological principle of minimum work I. The vascular system and the cost of blood volume. *Proceedings of the National Academy of Sciences*, 12(3):207–214, 1926.

[57] A Neic, M Liebmann, E Hoetzl, L Mitchell, E J Vigmond, G Haase, and G Plank. Accelerating cardiac bidomain simulations using graphics processing units. *IEEE Transactions on Biomedical Engineering*, 59:2281–2290, 2012.

[58] Aurel Neic, Fernando O. Campos, Anton J. Prassl, Steven A. Niederer, Martin J. Bishop, Edward J. Vigmond, and Gernot Plank. Efficient computation of electrograms and ECGs in human whole heart simulations using a reaction-eikonal model. *Journal of Computational Physics*, 346:191–211, 2017.

[59] Wilmer Nichols, Michael O'Rourke, and Charalambos Vlachopoulos. *McDonald's blood flow in arteries: theoretical, experimental and clinical principles*. CRC press, 2011.

[60] Steven Niederer, Lawrence Mitchell, Nicolas Smith, and Gernot Plank. Simulating human cardiac electrophysiology on clinical time-scales. *Frontiers in Physiology*, 2:14, 2011.

[61] Steven A. Niederer, Gernot Plank, Phani Chinchapatnam, Matthew Ginks, Pablo Lamata, Kawal S. Rhode, Christopher A. Rinaldi, Reza Razavi, and Nicolas P. Smith. Length-dependent tension in the failing heart and the efficacy of cardiac resynchronization therapy. *Cardiovascular Research*, 89(2):336, 2011.

[62] D Nordsletten, M McCormick, PJ Kilner, Peter Hunter, D Kay, and NP Smith. Fluid–solid coupling for the investigation of diastolic and systolic human left ventricular function. *International Journal for Numerical Methods in Biomedical Engineering*, 27(7):1017–1039, 2011.

[63] Pras Pathmanathan and JP Jonathan P. Whiteley. A numerical method for cardiac mechanoelectric simulations. *Ann. Biomed. Eng.*, 37(5):860–73, 2009.

[64] L. Pauli and M. Behr. On stabilized space-time FEM for anisotropic meshes: Incompressible Navier–Stokes equations and applications to blood flow in medical devices. *International Journal for Numerical Methods in Fluids*, pages 189–209, 2017.

[65] Alfio Quarteroni, Toni Lassila, Simone Rossi, and Ricardo Ruiz-Baier. Integrated Heart – Coupling multiscale and multiphysics models for the simulation of the cardiac function. *Comput. Methods Appl. Mech. Eng.*, 314(314):345–407, 2017.

[66] Kristóf Ralovich, Lucian Itu, Dime Vitanovski, Puneet Sharma, Razvan Ionasec, Viorel Mihalef, Waldemar Krawtschuk, Yefeng Zheng, Allen Everett, Giacomo Pongiglione, et al. Noninvasive hemodynamic assessment, treatment outcome prediction and follow-up of aortic coarctation from MR imaging. *Medical Physics*, 42(5):2143–2156, 2015.

[67] Bernardo M. Rocha, Ferdinand Kickinger, Anton J. Prassl, Gundolf Haase, Edward J. Vigmond, Rodrigo Weber dos Santos, Sabine Zaglmayr, and Gernot Plank. A macro finite-element formulation for cardiac electrophysiology simulations using hybrid unstructured grids. *IEEE Trans Biomed Eng*, 58(4):1055–1065, 2011.

[68] M. Schäfer, S. Turek, F. Durst, E. Krause, and R. Rannacher. *Benchmark Computations of Laminar Flow Around a Cylinder*, pages 547–566. Vieweg+Teubner Verlag, Wiesbaden, 1996.

[69] Torsten Schenkel, Mauro Malve, Michael Reik, Michael Markl, Bernd Jung, and Herbert Oertel. MRI-based CFD analysis of flow in a human left ventricle: methodology and application to a healthy heart. *Annals of Biomedical Engineering*, 37(3):503–515, 2009.

[70] M. Sellier. An iterative method for the inverse elasto-static problem. *Journal of Fluids and Structures*, 27(8):1461 – 1470, 2011.

[71] Jung Hee Seo and Rajat Mittal. Effect of diastolic flow patterns on the function of the left ventricle. *Physics of Fluids*, 25(11):110801, 2013.

[72] Jung Hee Seo, Vijay Vedula, Theodore Abraham, and Rajat Mittal. Multiphysics computational models for cardiac flow and virtual cardiography. *International Journal for Numerical Methods in Biomedical Engineering*, 29(8):850–869, 2013.

[73] David Silvester, Howard Elman, David Kay, and Andrew Wathen. Efficient preconditioning of the linearized Navier–Stokes equations for incompressible flow. *Journal of Computational and Applied Mathematics*, 128(1):261–279, 2001.

[74] Detlev Stalling, Malte Westerhoff, and Hans-Christian Hege. Amira: a highly interactive system for visual data analysis. In Charles D. Hansen and Chris R. Johnson, editors, *The Visualization Handbook*, pages 749–767. Elsevier, 2005.

[75] Olaf Steinbach. *Numerical approximation methods for elliptic boundary value problems: finite and boundary elements*. Springer Science & Business Media, 2007.

[76] Boyang Su, Ru San Tan, Ju Le Tan, Kenneth Wei Qiang Guo, Jun Mei Zhang, Shuang Leng, Xiaodan Zhao, John Carson Allen, and Liang Zhong. Cardiac MRI based numerical modeling of left ventricular fluid dynamics with mitral valve incorporated. *Journal of Biomechanics*, 49(7):1199–1205, 2016.

[77] P. Le Tallec and J. Mouro. Fluid structure interaction with large structural displacements. *Computer Methods in Applied Mechanics and Engineering*, 190(24):3039 – 3067, 2001.

[78] Dalin Tang, Chun Yang, Tal Geva, and J Pedro. Patient-specific MRI-based 3D FSI RV/LV/patch models for pulmonary valve replacement surgery and patch optimization. *Journal of Biomechanical Engineering*, 130(4):041010, 2008.

[79] Dalin Tang, Chun Yang, Tal Geva, and Pedro J. del Nido. Image-based patient-specific ventricle models with fluidâĂŞstructure interaction for cardiac function assessment and surgical design optimization. *Prog. Pediatr. Cardiol.*, 30(1-2):51–62, 2010.

[80] K H W J ten Tusscher, D Noble, P J Noble, and A V Panfilov. A model for human ventricular tissue. *American Journal of Physiology. Heart and Circulatory Physiology*, 286:H1573–H1589, 2004.

[81] The CGAL Project. *CGAL User and Reference Manual*. CGAL Editorial Board, 4.11 edition, 2017. URL `http://doc.cgal.org/4.11/Manual/packages.html`.

[82] R. van Loon, P.D. Anderson, F.N. van de Vosse, and S.J. Sherwin. Comparison of various fluidâĂŞstructure interaction methods for deformable bodies. *Computers & Structures*, 85 (11):833 – 843, 2007.

[83] M. Vázquez, R. Arís, J. Aguado-Sierra, G. Houzeaux, A. Santiago, M. López, P. Córdoba, M. Rivero, and J. C. Cajas. *Alya Red CCM: HPC-Based Cardiac Computational Modelling*, pages 189–207. Springer International Publishing, Cham, 2015.

[84] E. Vigmond, M. Hughes, G. Plank, and L. Leon. Computational tools for modeling electrical activity in cardiac tissue. *J Electrocardiol*, 36:69–74, 2003.

[85] E J Vigmond, R Weber dos Santos, A J Prassl, M Deo, and G Plank. Solvers for the cardiac bidomain equations. *Progress in Biophysics and Molecular Biology*, 96:3–18, 2008.

[86] Edward J. Vigmond, Clyde Clements, David M. McQueen, and Charles S. Peskin. Effect of bundle branch block on cardiac output: A whole heart simulation study. *Progress in Biophysics and Molecular Biology*, 97(2):520 – 542, 2008.

[87] Xiaodong Wang and Wing Kam Liu. Extended immersed boundary method using FEM and RKPM. *Computer Methods in Applied Mechanics and Engineering*, 193(12):1305 – 1321, 2004.

[88] Nicolaas Westerhof, GIJS Elzinga, and P Sipkema. An artificial arterial system for pumping hearts. *Journal of Applied Physiology*, 31(5):776–781, 1971.

[89] Ulrike Meier Yang et al. BoomerAMG: a parallel algebraic multigrid solver and preconditioner. *Applied Numerical Mathematics*, 41(1):155–177, 2002.

Tables

	Sex	Age	EDV	ESV	SV	EF	HR	CO	$P^{\text{dia}}_{\text{ao/cuff}}$	$P^{\text{sys}}_{\text{ao/cuff}}$	MAP	P_{open}
			ml	ml	ml	%	bpm	ml/s	mmHg	mmHg	mmHg	mmHg
28-Pre	F	9	88.2	30.6	57.54	65.3	91	87.46	$^{71.1}/_{62}$	$^{122.7}/_{138}$	$^{88.3}/_{87.3}$	71.33
44-Pre	M	12	91.7	31.6	60.09	65.5	76	76.31	$^{74.6}/_{120}$	$^{125.2}/_{154}$	$^{91.5}/_{131.3}$	74.78

Table 1: CoA patient characteristics from MRI and invasive catheter pressure recordings including end-diastolic volume (EDV), end-systolic volume (ESV), stroke volume (SV), ejection fraction (EF), heart rate (HR), cardiac output (CO), diastolic and systolic pressures recorded in the aorta or estimated from cuff measurements ($P_{\text{ao/cuff,dia}}$ and $P_{\text{ao/cuff,sys}}$), mean arterial pressure (MAP) computed from pressure recorded invasively in the aorta or estimated from $P_{\text{cuff,dia}}$ and $P_{\text{cuff,sys}}$, and aortic valve open pressure P_{open} determined from invasive pressure recordings.

Tag	**Label**
lv	Myocardium
ao	Aortic wall
cushion	Elastic cushion
av	Aortic valve
mv	Mitral valve
lvbp	Left ventricular bloodpool
aobp	Aortic bloodpool

Table 2: Labels used for defining the subdomains of $\Omega^0_{s,\text{total}}$.

	EM Fitting								
	S_{peak}	t_{dur}	τ_{c0}	τ_{r}	t_{emd}	C_{Guc}	R	Z	C
	kPa	ms	–	–	ms	kPa	kPa ms/ml	kPa ms/ml	ml/kPa
28-Pre	60.0	380	30.0	30.0	15.0	0.48	170.65	12.00	6.75
28-Post	55.0	380	30.0	30.0	15.0	0.48	170.65	12.00	6.75
44-Pre	90.0	400	50.0	50.0	15.0	0.48	166.65	13.33	7.42

Table 3: Fitted parameters for EM Model.

Name	Variable	Units	Expression / Value
Velocity	$\mathbf{u}_\mathrm{f}$	m/s	–
Pressure	p_f	Pa	–
Fluid stress tensor	$\boldsymbol{\sigma}_\mathrm{f}(\mathbf{u}_\mathrm{f}, p_\mathrm{f})$	Pa	$-p_\mathrm{f}\mathbf{I} + 2\mu_\mathrm{f}\boldsymbol{\varepsilon}(\mathbf{u}_\mathrm{f})$
Fluid density	ρ_f	kg/m^3	1060
Dynamic viscosity	μ_f	Pa s	0.004

Table 4: Physical parameters for the Navier–Stokes equations with their respective ranges and units. $\boldsymbol{\varepsilon}(\mathbf{u}_\mathrm{f})$ denotes the symmetric gradient defined as $\frac{1}{2}\left(\nabla_\mathbf{x}\mathbf{u}_\mathrm{f} + \nabla_\mathbf{x}\mathbf{u}_\mathrm{f}^\top\right)$

	EM Comparison					
	$\mathrm{EDV}_{\mathrm{cl,sim}}$ ml	$\mathrm{ESV}_{\mathrm{cl,sim}}$ ml	$\mathrm{SV}_{\mathrm{cl,sim}}$ ml	$\mathrm{EF}_{\mathrm{cl,sim}}$ %	$\mathrm{CO}_{\mathrm{cl,sim}}$ ml/s	$\mathrm{P}^{\mathrm{sys}}_{\mathrm{cl,sim}}$ mmHg
28-Pre	$^{88.16}/_{87.47}$	$^{30.62}/_{31.02}$	$^{57.54}/_{57.14}$	$^{65.27}/_{64.81}$	$^{87.46}/_{86.85}$	$^{146.037}/_{139.362}$
44-Pre	$^{91.68}/_{91.67}$	$^{31.59}/_{30.95}$	$^{60.10}/_{60.72}$	$^{65.54}/_{66.24}$	$^{76.31}/_{76.32}$	$^{158.413}/_{135.236}$
rel. error [%]	$^{0.78}/_{0.01}$	$^{1.3}/_{2.0}$	$^{0.69}/_{1.03}$	$^{0.70}/_{1.07}$	$^{0.69}/_{0.013}$	$^{4.57}/_{14.63}$

Table 5: Comparison of clinical indicators and indicators computed from simulation for the EM models.

	Electromechanics Model				CFD Model				
	NE	NV	h [µm]	DOF	NE	NV	h [µm]	DOFU	DOFP
28-Pre	747266	167509	897	502527	1943060	352006	746.5	1056018	352006
28-Post	632635	149174	954	447522	7405128	1294264	531.6	3882792	1294264
44-Pre	727194	168804	997	506412	2285005	412728	717	1238184	412728

Table 6: Discretization details for the studied cases. Shown are the number of elemens (NE), number of vertices (NV), average edge length h in µm, degrees of freedom for displacement (DOF), degrees of freedom for velocity (DOFU), degrees of freedom for pressure (DOFP).

	Outlet			
	DCA	BCA	RSC	LSC
R [kPa ms/ml]	590.46	264.6	1058.24	1058.24
Z [kPa ms/ml]	29.52	13.23	52.91	52.91
C [ml/kPa]	1.69	3.78	0.944	0.944

Table 7: Windkessel parameters for case *28-Pre*.

	Outlet			
	DCA	BCA	RSC	LSC
R [kPa ms/ml]	2480.07	276.01	466.23	7440.2
Z [kPa ms/ml]	124.003	13.9	23.31	372.01
C [ml/kPa]	0.403	3.62	2.14	0.134

Table 8: Windkessel parameters for case *44-Pre*.

Flux Comparison						
		28-Pre		*44-Pre*		
	Unit	$\varepsilon_{\mathrm{DCA}}$	$\varepsilon_{\mathrm{ASC}}$	$\varepsilon_{\mathrm{ASC}}$	$\varepsilon_{\mathrm{BCA}}$	$\varepsilon_{\mathrm{LSC}}$
$Q_{\mathrm{peak,sim}}$	ml/s	85.5073	286.056	316.713	160.493	132.540
$Q_{\mathrm{peak,cl}}$	ml/s	70.3071	290.719	352.114	171.571	109.290
rel. error	%	21.62	1.604	10.054	6.46	21.27

Table 9: Comparison of clincal estimated flow rates and simulated flow rates through the various planes for cases *28-Pre* and *44-Pre*.

Figures

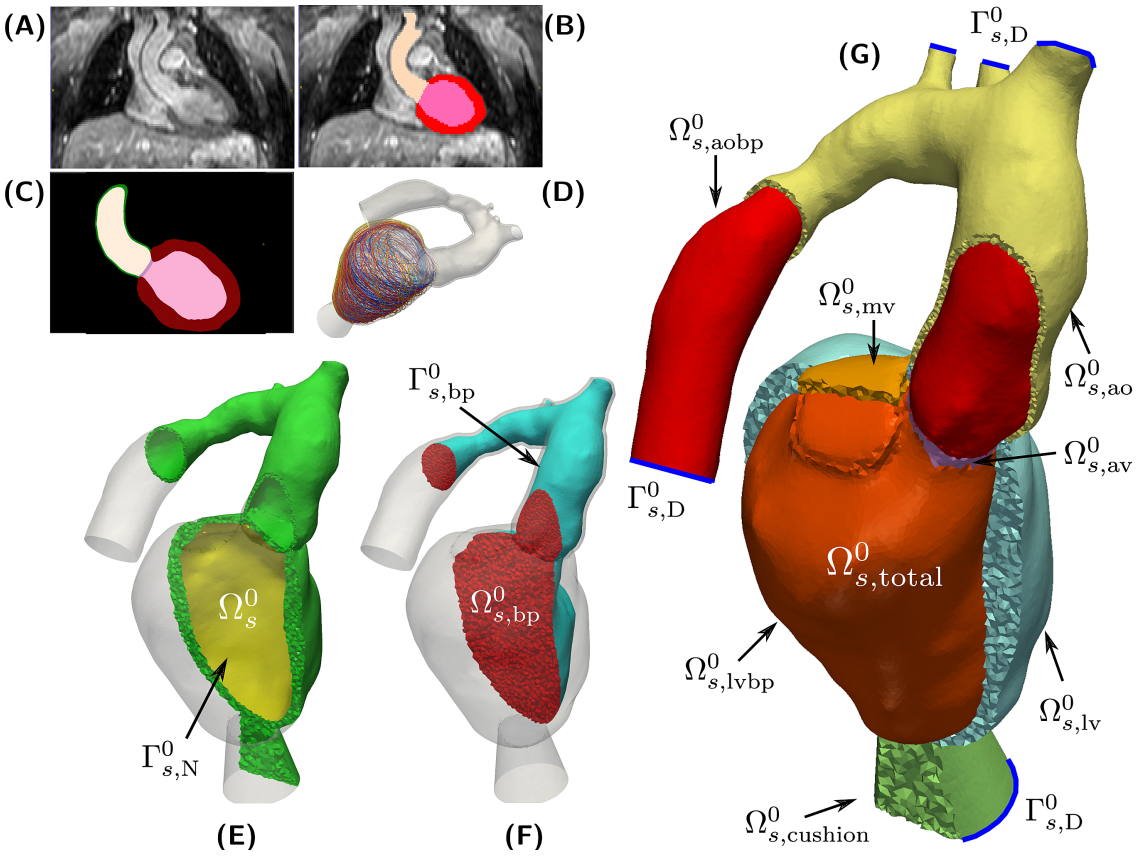

Figure 1: Mechanics model generation: Starting from a patient specific MRI scan (A) a segmentation was performed (B) which was then upsampled and smoothed (C). Myocardial fibers were generated in the tissue according to [10] (D). A labeled FE geometry $\Omega^0_{\mathrm{s,total}}$ including the blood pool was generated (G). The geometry has been sliced to reveal the blood pool and valves and has been color coded according to the labels defined in Table 2. Boundaries $\Gamma^0_{\mathrm{s,D}}$ used for prescribing homogeneous Dirichlet boundary conditions are sketched as blue curves. From this mesh the EM submesh Ω^0_{s} (E) and the unsmoothed blood pool (F) were extracted. Boundary $\Gamma^0_{\mathrm{s,N}}$ was used to prescribe pressure boundary conditions inside the LV and $\Gamma^0_{\mathrm{s,bp}}$ is the surface of the blood pool.

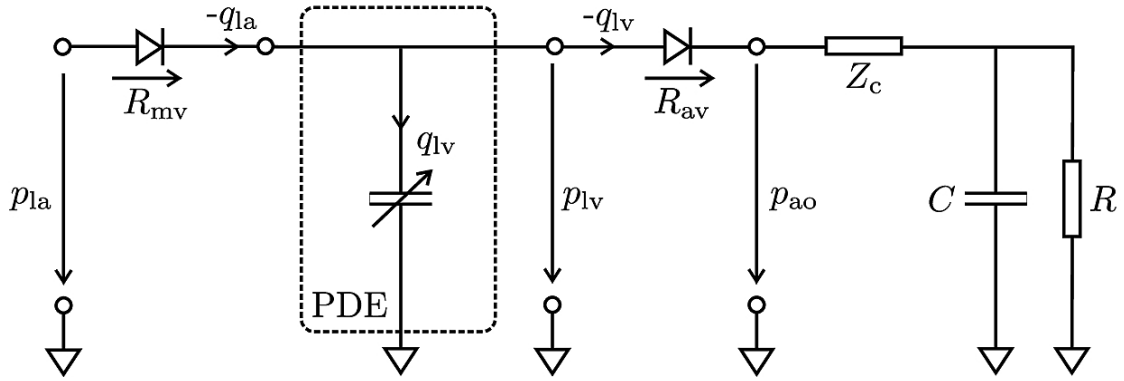

Figure 2: Lumped circuit representation of the coupled EM PDE model of the LV with the cardiovascular system. The time-varying compliance of the LV is represented as a PDE model which was coupled through the aortic valve (R_{av}) to a 3-element Windkessel model representing aortic impedance, Z_{c}, and peripheral arterial compliance, C, and resistance, R, during ejection, and through the mitral valve (R_{mv}) to a constant pressure p_{la} in the left atrium during filling. Negative flows $-q_{\mathrm{la}}$ and $-q_{\mathrm{lv}}$ mean the respective cavity is ejecting, while positive flow means cavity is being filled.

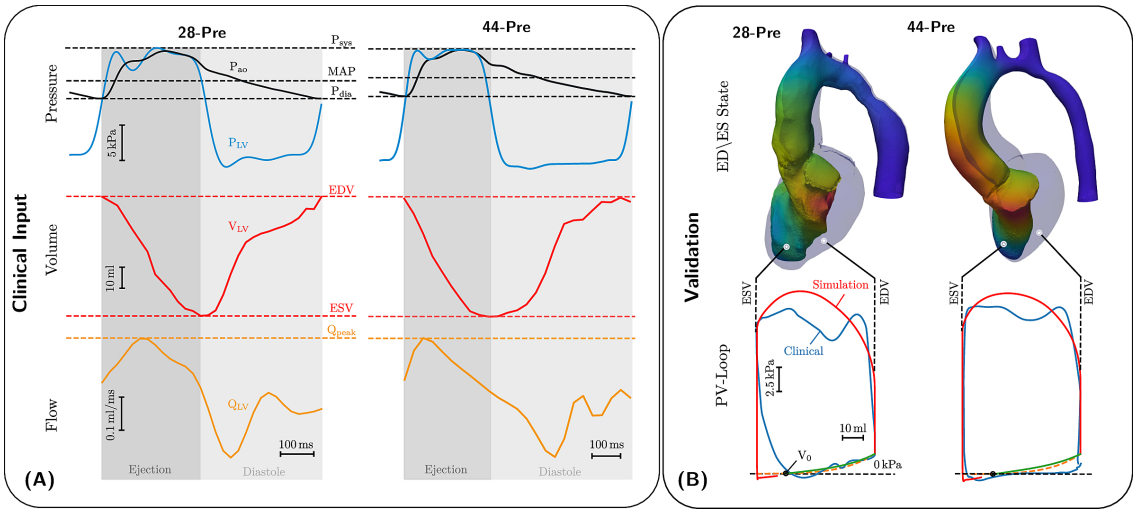

Figure 3: (A) Invasive clinical recordings from cases *28-Pre* and *44-Pre*. Top: Recorded aortic pressure $\mathrm{P_{ao}}$ (black curve) and recorded LV pressure $\mathrm{P_{LV}}$ (blue curve). Marked with dashed lines are Systolic pressure $\mathrm{P_{sys}}$, mean arterial pressure MAP, and diastolic pressure $\mathrm{P_{dia}}$; Center: Volume change in the LV, $\mathrm{V_{LV}}$, in red ranging from end-diastolic volume EDV to end-systolic volume ESV. Bottom: LV flow $\mathrm{Q_{LV}}$ in orange with marked peak flow $\mathrm{Q_{peak}}$. (B) Comparison of EM simulations and clinical data. Upper part shows a comparison of the LV model in end-diastolic (colored opaquley blue) and end-systolic configuration (colored by displacement). Lower part shows comparison of clinical (colored blue) and simulated PV loops (colored red). The dashed orange curve shows the ideal Klotz curve, while the green curve shows the simulated Klotz curve, with volume of stress-free unloaded configuration marked as $\mathrm{V_0}$.

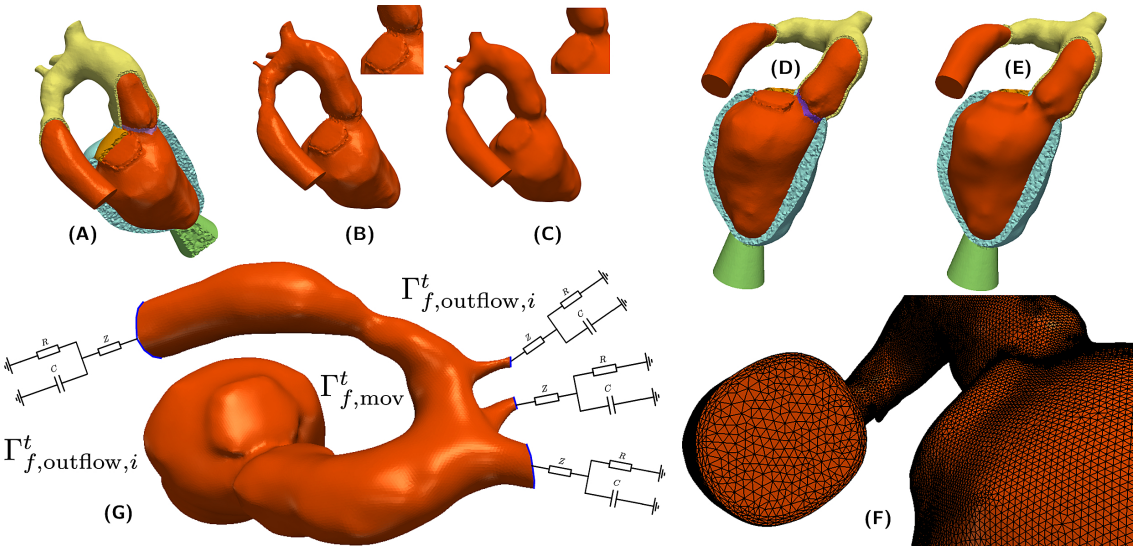

Figure 4: Processing workflow used for generating blood pool FE models: (A) and (B) Elements labeled as blood pool or valve were extracted from the mesh used for EM modeling. (C) Surfaces of extracted meshes were smoothed to avoid numerical instabilities due to reentrant corners resulting from a jagged surface. A closeup view of the smoothing effect is displayed in the upper right. The smoothed surface is then used as input for the fluid mesh generation. (D) and (E) Comparison of the smoothed and unsmoothed blood pool mesh immersed in the original EM mesh. (F) Closeup view of the generated boundary layer mesh. (G) Boundary conditions used for CFD. Moving wall boundary $\Gamma^t_{\text{f,mov}}$ colored in orange, outlet boundaries $\Gamma^t_{\text{f,outflow},i}$ colored in blue with attached illustration of the 3-element Windkessel models.

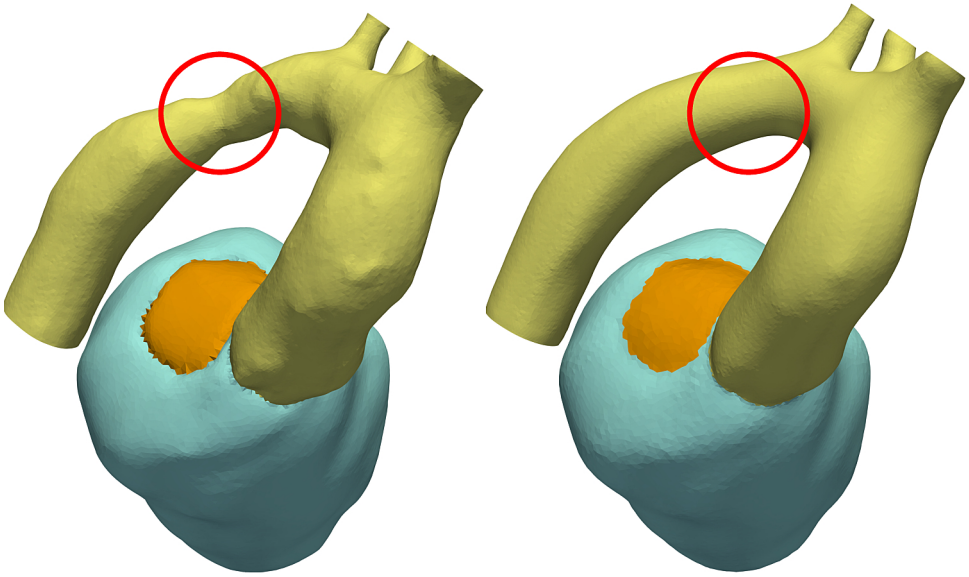

Figure 5: CoA anatomy of case 28 before and after virtual stenting procedure. CoA location is indicated with a red circle.

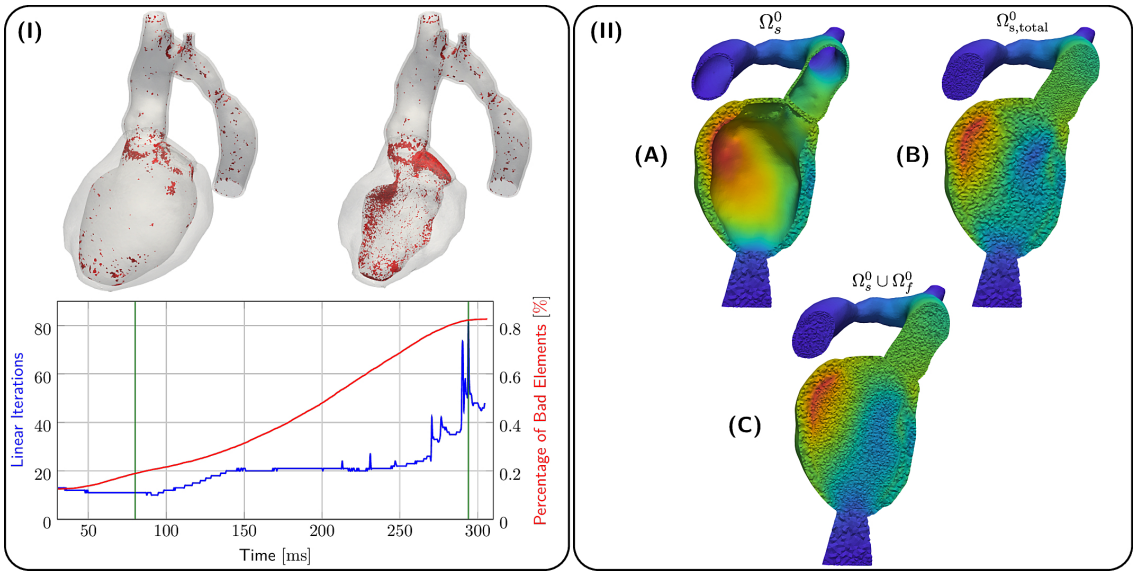

Figure 6: Panel (I) shows quality analysis for case *28-Pre*. Spatial locations of elements of poor quality > 0.8 (in red) are shown at the top for different snapshots of deformation (green lines in graph). The graph below shows linear iterations per time step (in blue) and percentage of elements with poor quality > 0.8 (in red). Panel (II) shows the processing stages of kinematic transfer for the *28-Pre* case at maximum displacement. (A) Displacement $\mathbf{d}_\text{s}$ on EM mesh Ω_s^0. (B) Displacement $\mathbf{d}_\text{s}$ extended to conformal EM blood pool mesh $\Omega_{\text{s,total}}^0$ which serves as hanging background mesh for the kinematic transfer onto the CFD blood pool mesh Ω_f^0. (C) Displacement $\mathbf{d}_\text{s}$ on Ω_s^0 superimposed with fluid mesh displacement $\mathbf{d}_\text{f}$ on Ω_f^0.

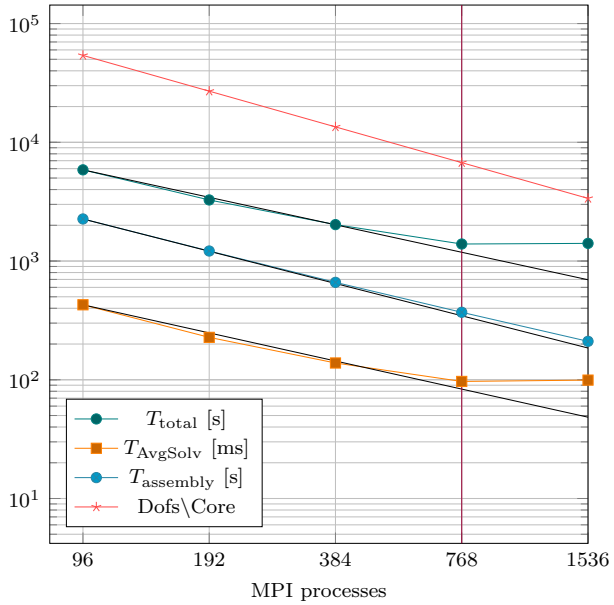

Figure 7: Results of strong scaling benchmark based on case *28-Post* with 5.2 million overall degrees of freedom. T_AvgSolv is the total solving time divided by the total amount of linear iterations per simulation run.

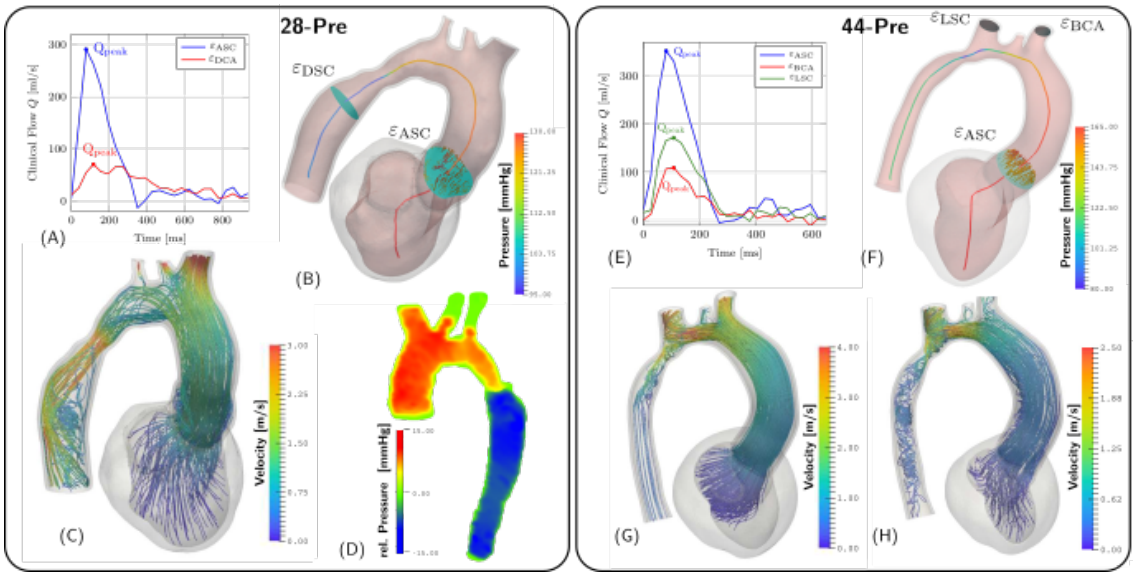

Figure 8: CFD results. Subfigures (A), (E) show the given clinical measurements for flow through different planes. The planes are depicted in Subfigures (B) and (F). Subfigures (B) and (F) also depict the pressure along the centerlines at peak flow conditions at $t = 167\,\text{ms}$ and $t = 142\,\text{ms}$ respectively. Subfigure (C) shows velocity streamlines at peak flow. Subfigure (D) shows the relative pressure map from the Pressure–Poisson mapping used for validating the pressure drop in our simulations. Subfigures (G), (H) show velocity streamlines at peak flow and $t = 200\,\text{ms}$ for case *44-Pre*.

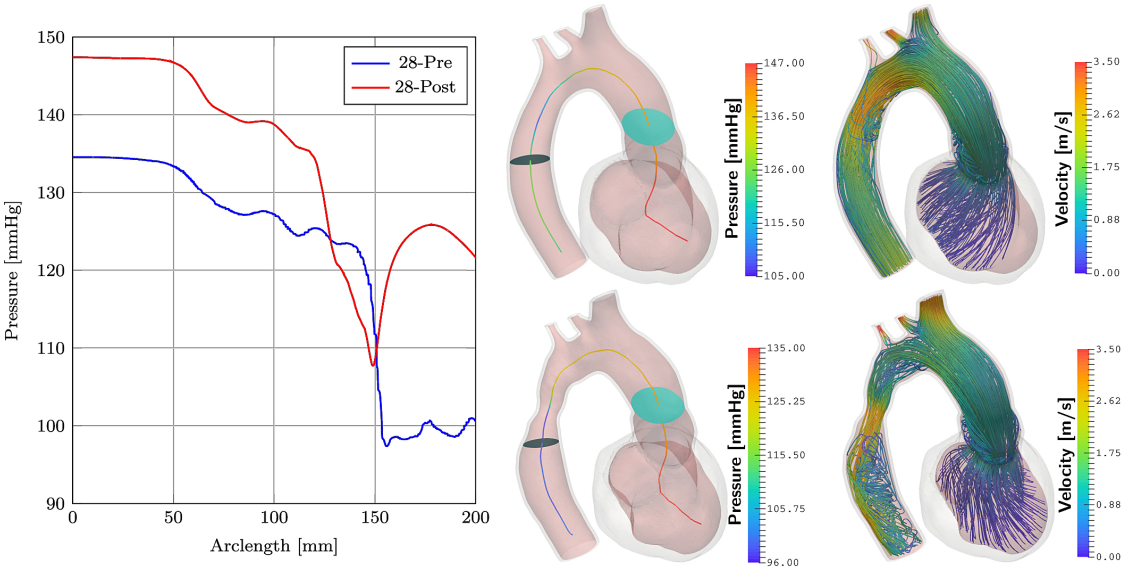

Figure 9: Comparison of cases *28-Pre* and *28-Post*. Shown on the left are the pressures along the centerline at peak flow. Depicted in the middle are the slices used for calculating the pressure drops. Shown on the right are velocity streamlines at peak flow.